Journal of Computational Physics 229 (2010) 4567–4590

Contents lists available at ScienceDirect

Journal of Computational Physics

journal homepage: www.elsevier.com/locate/jcp

A multi-moment finite volume formulation for shallow water equations on unstructured mesh

Ryosuke Akoh [a], Satoshi Ii [b], Feng Xiao [a,c,*]

[a] Department of Environmental Science and Technology, Tokyo Institute of Technology, 4259 Nagatsuta, Midori-ku, Yokohama 226-8502, Japan
[b] Department of Mechanical Engineering, The University of Tokyo, 7-3-1 Hongo Bunkyo-ku, Tokyo 113-8656, Japan
[c] LHD, Institute of Mechanics, Chinese Academy of Sciences, 15 Beisihuanxi Road, Beijing 100080, China

ARTICLE INFO

Article history:
Received 10 April 2009
Received in revised form 12 February 2010
Accepted 20 February 2010
Available online 9 March 2010

Keywords:
High order scheme
Finite volume method
Unstructured grid
Multi-moment
Shallow water equations
Hydraulic simulation

ABSTRACT

A novel and accurate finite volume method has been presented to solve the shallow water equations on unstructured grid in plane geometry. In addition to the volume integrated average (VIA moment) for each mesh cell, the point values (PV moment) defined on cell boundary are also treated as the model variables. The volume integrated average is updated via a finite volume formulation, and thus is numerically conserved, while the point value is computed by a point-wise Riemann solver. The cell-wise local interpolation reconstruction is built based on both the VIA and the PV moments, which results in a scheme of almost third order accuracy. Efforts have also been made to formulate the source term of the bottom topography in a way to balance the numerical flux function to satisfy the so-called C-property. The proposed numerical model is validated by numerical tests in comparison with other methods reported in the literature.

1. Introduction

Shallow water equations find a wide range of applications in hydraulic and coastal engineering. Due to the strong nonlinearity associated with free surface in nature, it is hard to obtain the analytical solutions to the shallow water equations except in rare simplified cases. Thus, computation turns up as an indispensable approach in the related fields. Numerical techniques of shallow water model have been devoted a lot of efforts so far, and as a consequence, many numerical models have been developed for scientific researches and engineering applications. In real case simulations, unstructured mesh (or grid) is getting more and more popular in the community to represent the complex geometries of river bank and coastal line.

Conventional finite volume shock-capturing method with unstructured mesh has been proved successful in solving shallow water equations with complex geometrical boundary. Zhao et al. [44] used the finite volume method (FVM) with Osher's scheme to solve the local 1D Riemann problem across the boundary of unstructured mesh element that is either triangular or quadrilateral. A first-order formulation was built using a cell-averaged piece-wise constant reconstruction. Wang and Liu [33] blended two central schemes, i.e. Lax-Wendroff scheme and Lax-Friedrich scheme to get a stable and efficient formulation on triangular meshes. FVMs of second-order accuracy for shallow water model based on flux-vector splitting and flux-difference splitting were reported in Anastasiuo and Chan [2], Burguete and Navarro [7], Lin et al. [23] and Brufau et al. [6]. Erduran et al. [11] evaluated and reviewed some existing approximate Riemann solvers for shallow water equations.

More recently, high-order schemes using local reconstructions, which are well suitable for building high-order numerical models on unstructured grids, have drawn great attention of researchers, and numerical techniques of this sort, such as

* Corresponding author. Address: LHD, Institute of Mechanics, Chinese Academy of Sciences, 15 Beisihuanxi Road, Beijing 100080, China. Tel./fax: +86 10 82543877.
E-mail addresses: xiao@es.titech.ac.jp, xiao@imech.ac.cn (F. Xiao).

0021-9991/$ - see front matter © 2010 Elsevier Inc. All rights reserved.
doi:10.1016/j.jcp.2010.02.023

discontinuous Galerkin (DG) method [12,3,41,15] and spectral volume (SV) method [9] have been implemented in solving shallow water equations.

Different from other existing schemes, a new type method, namely Constrained Interpolated Profile/Multi-Moment Finite Volume Method or shortly CIP/MM FVM, has been recently developed. The basic idea of the CIP/MM FVM is to make use of the cell-averaged value and the point value or even other kinds of discretized quantities simultaneously as the model variables (unknowns) which need to be memorized and predicted at every time step. The method has been implemented in different forms to compute various fluid flows [34–37,19]. Having different moments defined over a compact stencil (in fact the reconstruction can be built over single cell in most cases), a multi-moment finite volume method can be easily extended to unstructured grid. Ii et al. [18] devised a 4th-order scheme for scalar transport equation on a triangular unstructured grid using a semi-Lagrangian updating procedure.

The multi-moment FVM has also been implemented to shallow water equations in structured grids. Akoh et al. [1] used a semi-Lagrangian solution procedure to compute the point values located on the cell boundary based on the characteristic theory of the shallow water equations, and the topographic source term is formulated in balance to the numerical flux to satisfy the so-called C-property. Chen and Xiao [8] updated the point values at cell boundary using point-wise Riemann solver given the multi-moment reconstructions based on both cell-averaged value and point value. A global shallow water model has been constructed on a cubed spherical coordinate generated from a gnomonic projection.

In this paper, we propose a new numerical model for shallow water equations on unstructured mesh using the multi-moment concept and the point-wise Riemann solver. In the current model, we define two kinds of moments, i.e. volume integrated average (VIA) and point values (PVs), and treat them as the model variables to be predicted at every time step. The VIA moments are computed through a finite volume formulation of flux form, while the PVs are updated by solving the local Riemann problems in terms of the derivatives at points on the cell boundary. Moreover, the numerical formulation is devised so that the source terms are well balanced to the fluxes on the discretized level for both VIA and PV moments.

The paper is organized as follows. In Section 2, we describe at first the multi-moment finite volume formulation with local approximate Riemann solver to update the PVs for one dimensional hyperbolic equation. Then the formulation of two dimensions are extended to unstructured triangular grid. The formulation of shallow water equations is presented in Section 3 with details. Section 4 gives numerical results including some widely used benchmark tests to evaluate the proposed method from various aspects, particularly on the convergence rate (order of accuracy), the capability in capturing discontinuous wave fronts, as well as the computation of flows with irregular bottom topography. Finally, we end up with some concluding remarks in Section 5.

2. Multi-moment finite volume method

2.1. Basic formulation in one dimension

In this section, we describe the numerical formulation of the multi-moment finite volume method for the one dimensional hyperbolic equation as follows:

$$\frac{\partial q}{\partial t}+\frac{\partial F(q)}{\partial x}=0, \tag{2.1}$$

where $q(x,t)$ is the conservative variable and $F(q(x,t))$ the flux function.

Assuming that the computational domain is partitioned into I mesh cells, the ith cell is bounded by $[x_{i-1/2},x_{i+1/2}]$ with $i=1,2,\ldots,I$. In this paper, we define the following two kinds of moments for $q(x,t)$, and treat them as the model variables independently.

- VIA (volume integrated average) :

$$\overline{{}^{V}q}_i(t)\equiv\frac{1}{\Delta x_i}\int_{x_{i-1/2}}^{x_{i+1/2}}q(x,t)dx, \tag{2.2}$$

- PV (point value) :

$$\overline{Pq}_{i+\frac{1}{2}}(t)\equiv q(x_{i+\frac{1}{2}},t), \tag{2.3}$$

where $\Delta x_i=x_{i+1/2}-x_{i-1/2}$ denotes the grid size and Fig. 1 shows the location of moments.

Using multiple moments allows us to construct the high-order interpolation function with a single cell[28,42,38,39]. To remove the numerical oscillations associating the discontinuous solutions, we adopt the cubic interpolation function previously used in the CIP-Conservative Semi-Lagrangian with cubic polynomial (CIP-CSL3) scheme [38]. The one dimensional piecewise cubic interpolation function on cell i is given by

$$\mathcal{Q}_i(x)=a_3(x-x_{i-\frac{1}{2}})^3+a_2(x-x_{i-\frac{1}{2}})^2+a_1(x-x_{i-\frac{1}{2}})+a_0. \tag{2.4}$$

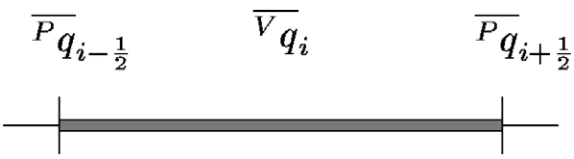

Fig. 1. The definition of moments on 1D cell i.

In order to determine the set of coefficients $a_0,\ldots,a_3$ uniquely, we need four constrained conditions for each cell stencil. The CIP-CSL3 type scheme uses two PVs at the cell boundaries, one VIA over the cell and the first order derivative d_i at the cell center as the constraints,

$$\begin{cases} \mathcal{Q}_i(x_{i-\frac{1}{2}}) = a_0 = \overline{P}q_{i-\frac{1}{2}}, \\ \mathcal{Q}_i(x_{i+\frac{1}{2}}) = a_3(\Delta x_i)^3 + a_2(\Delta x_i)^2 + a_1\Delta x_i + a_0 = \overline{P}q_{i+\frac{1}{2}}, \\ \frac{1}{\Delta x_i}\int_{x_{i-\frac{1}{2}}}^{x_{i+\frac{1}{2}}} \mathcal{Q}_i(x)dx = \frac{1}{4}a_3(\Delta x_i)^3 + \frac{1}{3}a_2(\Delta x_i)^2 + \frac{1}{2}a_1\Delta x_i + a_0 = \overline{V}q_i, \\ \left.\frac{d\mathcal{Q}_i(x)}{dx}\right|_{x=x_i} = \frac{3}{4}a_3(\Delta x_i)^2 + a_2\Delta x_i + a_1 = d_i. \end{cases} \tag{2.5}$$

The first-order derivatives d_i is not a prognostic variable but approximated from PV and VIA moments [38], and serves as a parameter to control the interpolation function and remove numerical oscillations. Some choices of d_i for practical use can be found in [38]. It is straightforward that if we use a second-order approximation for d_i simply from a central differencing of cell boundary point values $\overline{P}\phi_{i-1/2}$ and $\overline{P}\phi_{i+1/2}$ of cell i,

$$d_i = \frac{\overline{P}\phi_{i+\frac{1}{2}} - \overline{P}\phi_{i-\frac{1}{2}}}{\Delta x_i}, \tag{2.6}$$

the coefficient of the third-order term in (2.4) will vanish, and the cubic interpolation function becomes a quadratic one. In this case one can get a third order accuracy. More importantly, the first order derivative at the cell center d_i can effectively work as a slope limiter to control the numerical oscillations in the solution. We in the present work use a formula widely adopted in other high resolution schemes [29,10],

$$d_i = \begin{cases} \min(|\sigma_l|,|\sigma_c|,|\sigma_r|), & \text{if } \sigma_l\cdot\sigma_r > 0 \\ 0, & \text{otherwise}, \end{cases} \tag{2.7}$$

where

$$\sigma_l = \frac{(\overline{V}q_i - \overline{V}q_{i-1})}{(x_i - x_{i-1})}, \quad \sigma_c = \frac{(\overline{P}q_{i+\frac{1}{2}} - \overline{P}q_{i-\frac{1}{2}})}{(x_{i+\frac{1}{2}} - x_{i-\frac{1}{2}})} \quad \text{and} \quad \sigma_r = \frac{(\overline{V}q_{i+1} - \overline{V}q_i)}{(x_{i+1} - x_i)}.$$

As can be seen from the numerical results, (2.7) effectively suppresses numerical oscillations around discontinuities of water front. Shown in [36], parameter d_i can be also used to reduce the numerical diffusion error, and thus to steepen a gradient in numerical solution.

We should note here two major features of the multi-moment finite volume formulation presented in this paper that differ substantially from other methods in controlling numerical oscillations. (1) The slope limiter is incorporated into the piece-wise cubic reconstruction function as a constraint, whereas in other methods the interpolation function is usually degraded to a linear function with the slope calculated from a limiting procedure. (2) The point value (PV moment) at the cell boundary remains continuous, not like in the other schemes where the values at the two sides of the cell boundary are usually broken. In this sense, the present method employs a "soft" limiting projection for enhancing the numerical monotonicity compared to those used in most existing methods. Nevertheless, this simple limiting effectively removes the spurious numerical oscillations as will be shown in the numerical test section.

From (2.5), the coefficients read

$$\begin{aligned} a_0 &= \overline{P}q_{i-\frac{1}{2}}, \\ a_1 &= \frac{2\left(3\overline{V}q_i - 3\overline{P}q_{i-\frac{1}{2}} + \Delta x_i d_i\right)}{\Delta x_i}, \\ a_2 &= \frac{3\left(-2\overline{V}q_i - \overline{P}q_{i+\frac{1}{2}} + 3\overline{P}q_{i-\frac{1}{2}} + 2\Delta x_i d_i\right)}{\Delta x_i^2}, \\ a_3 &= \frac{4\left(\overline{P}q_{i+\frac{1}{2}} - \overline{P}q_{i-\frac{1}{2}} - \Delta x_i d_i\right)}{\Delta x_i^3}. \end{aligned} \tag{2.8}$$

In the scheme based on the multi-moment concept, different moments can be temporally updated by different approaches. In the present formulation, the PVs, which need not to be rigorously conserved, are updated by solving the local Riemann problems in terms of the derivatives of flux function at each discrete point. On the other hand, the VIA is updated by the finite volume formulation of flux-form to maintain the numerical conservation. As discussed later, the numerical fluxes are computed by using the PVs readily updated on the boundary of the control volume.

In practice, the semi-discretized evolution equations for updating PV and VIA moments, defined by (2.2) and (2.3), are derived from (2.1) as,

- PV:

$$\frac{d\overline{{}^{P}q}_{i+\frac{1}{2}}}{dt} = -\partial_x \mathcal{F}_{i+\frac{1}{2}}, \tag{2.9}$$

- VIA:

$$\frac{d\overline{{}^{V}q}_{i}}{dt} = -\frac{1}{\Delta x_i}\left(\mathcal{F}_{i+\frac{1}{2}} - \mathcal{F}_{i-\frac{1}{2}}\right), \tag{2.10}$$

where $\mathcal{F} = F(q)$ and $\partial_x \mathcal{F} = \partial F(q)/\partial x$ denote the consistent numerical formulations for the flux function and its first-order derivative, respectively.

The interpolation reconstruction is carried out piece-wisely with (2.4). It is obvious that the interpolation functions over two neighboring cells share the same point value at the cell boundary, i.e.

$$\mathcal{Q}_i\left(x_{i+\frac{1}{2}}\right) = \mathcal{Q}_{i+1}\left(x_{i+\frac{1}{2}}\right) = \overline{{}^{P}q}_{i+\frac{1}{2}}. \tag{2.11}$$

The first order derivative at cell boundary, however, may not be continuous. Here, we denote the first order derivative of the state variable on the left side of cell boundary $x_{i+1/2}$ as $\partial_x q^-_{i+1/2}$ and that on the right side as $\partial_x q^+_{i+1/2}$, respectively. The derivative of the state variable at cell boundary is then written as,

$$\partial_x q\left(x_{i+\frac{1}{2}}\right) = \begin{cases} \partial_x q^-_{i+\frac{1}{2}} & \text{if } x < x_{i+\frac{1}{2}}, \\ \partial_x q^+_{i+\frac{1}{2}} & \text{if } x > x_{i+\frac{1}{2}}, \end{cases} \tag{2.12}$$

where $\partial_x q^-_{i+1/2}$ and $\partial_x q^+_{i+1/2}$ are computed from the two neighboring piecewise reconstructions $\mathcal{Q}(x)$ separately by

$$\partial_x q^-_{i+\frac{1}{2}} = \left.\frac{\partial \mathcal{Q}_i(x)}{\partial x}\right|_{x_{i+\frac{1}{2}}} \quad \text{and} \quad \partial_x q^+_{i+\frac{1}{2}} = \left.\frac{\partial \mathcal{Q}_{i+1}(x)}{\partial x}\right|_{x_{i+\frac{1}{2}}}. \tag{2.13}$$

The numerical formulation required in (2.9) for updating the PV moment is then computed by the following LLF (local Lax-Friedrichs) approximate Riemann solver [27],

$$\partial_x \mathcal{F}_{i+\frac{1}{2}} = \frac{1}{2}\left\{\partial_x F\left(\partial_x q^-_{i+\frac{1}{2}}\right) + \partial_x F\left(\partial_x q^+_{i+\frac{1}{2}}\right) - \alpha_{i+\frac{1}{2}}\left(\partial_x q^+_{i+\frac{1}{2}} - \partial_x q^-_{i+\frac{1}{2}}\right)\right\}, \tag{2.14}$$

where $\partial_x F(\partial_x q^{\pm}_{i+1/2})$ denote the first order derivatives of the flux function computed from the values obtained by (2.13), and $\alpha_{i+1/2} = (\partial F/\partial q)_{i+1/2}$ is the largest eigen value computed by the PVs defined at the cell boundary. A more robust alternative is to specify $\alpha_{i+1/2}$ as the largest eigen value of $(\partial F/\partial q)$ in the two neighboring cells $[x_{i-1/2}, x_{i+1/2}]$ and $[x_{i+1/2}, x_{i+3/2}]$.

With the PV moments at cell boundary $\overline{{}^{P}q}_{i+\frac{1}{2}}$ updated by (2.9), the numerical flux in (2.10) can be directly obtained by $\mathcal{F}_{i+\frac{1}{2}} = F\left(\overline{{}^{P}q}_{i+\frac{1}{2}}\right)$, which does not require the numerical procedure for solving the Riemann problem and is thus computationally efficient.

Given the spatial discretizations of $\partial_x \mathcal{F}_{i+\frac{1}{2}}$ and $\mathcal{F}_{i+\frac{1}{2}}$, we use the third-order TVD (Total Variation Diminishing) Runge-Kutta method [26] to solve the semi-discretized system, (2.9) and (2.10). The time integration for PVs is then computed by

$$\begin{aligned}
&\overline{{}^{P}q}^{\langle 0\rangle}_{i+\frac{1}{2}} \equiv \overline{{}^{P}q}^{n}_{i+\frac{1}{2}}, \\
&\overline{{}^{P}q}^{\langle 1\rangle}_{i+\frac{1}{2}} = \overline{{}^{P}q}^{\langle 0\rangle}_{i+\frac{1}{2}} - \partial_x \mathcal{F}^{\langle 0\rangle}_{i+\frac{1}{2}}\Delta t, \\
&\overline{{}^{P}q}^{\langle 2\rangle}_{i+\frac{1}{2}} = \frac{3}{4}\overline{{}^{P}q}^{\langle 0\rangle}_{i+\frac{1}{2}} + \frac{1}{4}\overline{{}^{P}q}^{\langle 1\rangle}_{i+\frac{1}{2}} - \frac{1}{4}\partial_x \mathcal{F}^{\langle 1\rangle}_{i+\frac{1}{2}}\Delta t, \\
&\overline{{}^{P}q}^{\langle 3\rangle}_{i+\frac{1}{2}} = \frac{1}{3}\overline{{}^{P}q}^{\langle 0\rangle}_{i+\frac{1}{2}} + \frac{2}{3}\overline{{}^{P}q}^{\langle 2\rangle}_{i+\frac{1}{2}} - \frac{2}{3}\partial_x \mathcal{F}^{\langle 2\rangle}_{i+\frac{1}{2}}\Delta t, \\
&\overline{{}^{P}q}^{n+1}_{i+\frac{1}{2}} = \overline{{}^{P}q}^{\langle 3\rangle}_{i+\frac{1}{2}},
\end{aligned} \tag{2.15}$$

where $\overline{{}^{P}q}^{\langle l\rangle}$ (with $l = 0, 1, 2, 3$) denotes the PVs at the lth Runge-Kutta sub-step and $\partial_x \mathcal{F}^{\langle l\rangle}$ the corresponding numerical flux in terms of the derivatives computed by the piecewise reconstructions given above.

Likewise, the time integration for VIA is computed by

$$\begin{aligned}
\overline{{}^{V}q}_i^{\langle 0\rangle} &\equiv \overline{{}^{V}q}_i^{n},\\
\overline{{}^{V}q}_i^{\langle 1\rangle} &= \overline{{}^{V}q}_i^{\langle 0\rangle} - \frac{1}{\Delta x_i}\left(\mathcal{F}^{\langle 0\rangle}_{i+\frac{1}{2}} - \mathcal{F}^{\langle 0\rangle}_{i-\frac{1}{2}}\right)\Delta t,\\
\overline{{}^{V}q}_i^{\langle 2\rangle} &= \frac{3}{4}\overline{{}^{V}q}_i^{\langle 0\rangle} + \frac{1}{4}\overline{{}^{V}q}_i^{\langle 1\rangle} - \frac{1}{4}\frac{1}{\Delta x_i}\left(\mathcal{F}^{\langle 1\rangle}_{i+\frac{1}{2}} - \mathcal{F}^{\langle 1\rangle}_{i-\frac{1}{2}}\right)\Delta t,\\
\overline{{}^{V}q}_i^{\langle 3\rangle} &= \frac{1}{3}\overline{{}^{V}q}_i^{\langle 0\rangle} + \frac{2}{3}\overline{{}^{V}q}_i^{\langle 2\rangle} - \frac{2}{3}\frac{1}{\Delta x_i}\left(\mathcal{F}^{\langle 2\rangle}_{i+\frac{1}{2}} - \mathcal{F}^{\langle 2\rangle}_{i-\frac{1}{2}}\right)\Delta t,\\
\overline{{}^{V}q}_i^{n+1} &= \overline{{}^{V}q}_i^{\langle 3\rangle},
\end{aligned} \tag{2.16}$$

where $\overline{{}^{V}q}^{\langle l\rangle}$ (with $l = 0,1,2,3$) stands for the VIA at the lth Runge-Kutta sub-step and $\mathcal{F}^{\langle l\rangle}$ the numerical flux computed directly from the PV moment ($\overline{{}^{P}q}^{\langle l\rangle}$) at cell boundary.

2.2. Some remarks

When the multi-moment reconstruction (2.4) and (2.8) has been built, the PV moment can be updated by either a semi-Lagrangian procedure [19,1] or a complete Eulerian approach with the point-wise Riemann solver, like (2.9) for example. We have shown in [19] that a parabolic reconstruction (CIP-CSL2 [42]) combined with a third order Runge-Kutta time marching scheme gives third order accuracy in both space and time. As discussed previously, in the present work we devise a multi-moment spatial discretization at first to get a semi-discretized system, i.e. (2.9) and (2.10), and then use the Runge-Kutta time integration scheme (2.15) and (2.16) to update the unknowns as other high resolution schemes where DG or high order finite volume methods, for example, are used as their building block of the spatial discretization. So, it is obvious that the numerical accuracy of the present method is determined by the multi-moment discretization in space and the Runge-Kutta scheme in time. By separating the numerical treatments of space and time as a Eulerian approach, the numerical formulation presented in this paper is more easy to use, especially in multi-dimensional case. As will be shown later, the present formulation can obtain a third order accuracy on unstructured triangular mesh.

The present formulation also provides the user great flexibility and freedom to choose other existing schemes for the derivative Riemann problem and time integration as the building blocks. In this sense, one can build a model by using the multi-moment formulation as part of his numerical recipe.

Concerning the computational efficiency, we address two major advantages that make the present method more favorable. (1) The PV moment is located at the cell boundary and thus shared by the two neighboring cells, so a multi-moment finite volume formulation requires less unknowns (degrees of freedom) compared to other methods of the same order in which the unknowns are defined inside each cell separately, and (2) our numerical tests show that the maximum allowable CFL number for computational stability of present method is 0.411, which is larger compared to the third order schemes of DG and SV methods reported in [43]. These advantages are more significant in multi-dimensions.

2.3. Formulation on unstructured triangular grid

In this section, we describe the implementation of the multi-moment finite volume formulation on unstructured triangular grid. We first consider a two dimensional scalar hyperbolic conservation law given by

$$\frac{\partial q}{\partial t} + \frac{\partial F(q)}{\partial x} + \frac{\partial G(q)}{\partial y} = 0, \tag{2.17}$$

where $F(q)$ and $G(q)$ denote the flux functions of hyperbolicity in x and y-directions, respectively.

For triangular cell i, we define its vertexes as $v_{ij} \equiv (x_{ij}, y_{ij})$, $(j = 1,2,3)$ and boundary lines as $l_{i1} = \overline{v_{i2}v_{i3}}, l_{i2} = \overline{v_{i3}v_{i1}}, l_{i3} = \overline{v_{i1}v_{i2}}$. We denote the outward normal unit vector of boundary line segment l_{ij}, $j = 1,2,3$, by $\mathbf{n}_{ij} = (n_{xij}, n_{yij}) = n_{xij}\mathbf{e}_x + n_{yij}\mathbf{e}_y$, where $\mathbf{e}_x$ and $\mathbf{e}_y$ are the unit vectors in x and y-directions. Additionally, we define the middle point on boundary lines l_{i1}, l_{i2} and l_{i3} as m_{i1}, m_{i2} and m_{i3}.

The area Δs_i of cell i is computed by

$$\Delta s_i = \frac{1}{2}\begin{vmatrix} x_{i1} & y_{i1} & 1\\ x_{i2} & y_{i2} & 1\\ x_{i3} & y_{i3} & 1 \end{vmatrix}, \tag{2.18}$$

and the length of line segments Δl_{ij} $(j = 1,2,3)$ are given by

$$\Delta l_{i1} = \sqrt{(x_{i3} - x_{i2})^2 + (y_{i3} - y_{i2})^2}, \tag{2.19}$$

$$\Delta l_{i2} = \sqrt{(x_{i1} - x_{i3})^2 + (y_{i1} - y_{i3})^2}, \tag{2.20}$$

$$\Delta l_{i3} = \sqrt{(x_{i2} - x_{i1})^2 + (y_{i2} - y_{i1})^2}. \tag{2.21}$$

We define the VIA over the control volume, and the PVs at the vertexes as well as the middle points of each boundary edges for the state variable q as depicted in Fig. 2.

The moments are then written as

- VIA :

$$\overline{{}^{V}q}_i \equiv \frac{1}{\Delta s_i}\int_{s_i} q(x,y,t)ds, \tag{2.22}$$

- PV (vertex v_{ij}) :

$$\overline{{}^{P_v}q}_{ij} \equiv q(v_{ij},t) \quad (j=1,2,3), \tag{2.23}$$

- PV (middle point of boundary m_{ij}) :

$$\overline{P_m q}_{ij} \equiv q(m_{ij},t) \quad (j=1,2,3), \tag{2.24}$$

where s_i stands for the region of cell i.

We construct the two dimensional piecewise quadratic interpolation function over each cell element.

Similar to [18], we use the local area coordinate for the interpolation reconstruction. Shown in Fig. 3, the local area coordinate for triangular element i can be defined through the following relationships between the original Cartesian coordinate (x,y) and the area coordinate (L_1, L_2, L_3).

$$\begin{pmatrix} x \\ y \\ 1 \end{pmatrix} = \begin{pmatrix} x_{i1} & x_{i2} & x_{i3} \\ y_{i1} & y_{i2} & y_{i3} \\ 1 & 1 & 1 \end{pmatrix} \begin{pmatrix} L_1 \\ L_2 \\ L_3 \end{pmatrix}, \tag{2.25}$$

$$\begin{pmatrix} L_1 \\ L_2 \\ L_3 \end{pmatrix} = \frac{1}{J_i} \begin{pmatrix} y_{i2}-y_{i3} & x_{i3}-x_{i2} & x_{i2}y_{i3}-x_{i3}y_{i2} \\ y_{i3}-y_{i1} & x_{i1}-x_{i3} & x_{i3}y_{i1}-x_{i1}y_{i3} \\ y_{i1}-y_{i2} & x_{i2}-x_{i1} & x_{i1}y_{i2}-x_{i2}y_{i1} \end{pmatrix} \begin{pmatrix} x \\ y \\ 1 \end{pmatrix}, \tag{2.26}$$

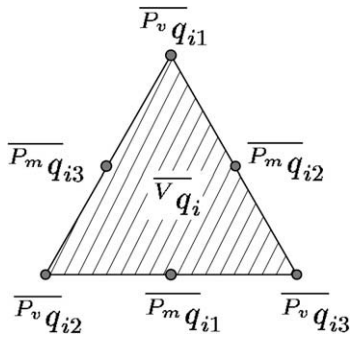

Fig. 2. The definition of moments on 2D cell i.

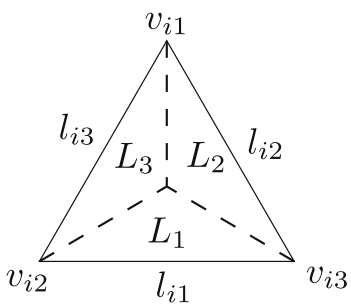

Fig. 3. The area coordinate for cell i.

where J_i is the transformation metric and given by

$$J_i = 2\Delta s_i = \begin{vmatrix} x_{i1} & y_{i1} & 1 \\ x_{i2} & y_{i2} & 1 \\ x_{i3} & y_{i3} & 1 \end{vmatrix}. \tag{2.27}$$

Consequently, the transformation of the derivatives between the two coordinate systems read

$$\begin{cases} \frac{\partial}{\partial x} = \frac{\partial L_1}{\partial x}\frac{\partial}{\partial L_1} + \frac{\partial L_2}{\partial x}\frac{\partial}{\partial L_2} + \frac{\partial L_3}{\partial x}\frac{\partial}{\partial L_3}, \\ \quad = \frac{y_{i2}-y_{i3}}{J_i}\frac{\partial}{\partial L_1} + \frac{y_{i3}-y_{i1}}{J_i}\frac{\partial}{\partial L_2} + \frac{y_{i1}-y_{i2}}{J_i}\frac{\partial}{\partial L_3}, \\ \frac{\partial}{\partial y} = \frac{\partial L_1}{\partial y}\frac{\partial}{\partial L_1} + \frac{\partial L_2}{\partial y}\frac{\partial}{\partial L_2} + \frac{\partial L_3}{\partial y}\frac{\partial}{\partial L_3} \\ \quad = \frac{x_{i3}-x_{i2}}{J_i}\frac{\partial}{\partial L_1} + \frac{x_{i1}-x_{i3}}{J_i}\frac{\partial}{\partial L_2} + \frac{x_{i2}-x_{i1}}{J_i}\frac{\partial}{\partial L_3}. \end{cases} \tag{2.28}$$

The quadratic interpolation function over cell i is then written in the area coordinate system as follows:

$$\mathcal{Q}_i(L_1, L_2, L_3) = a_1L_1 + a_2L_2 + a_3L_3 + a_4L_1L_2 + a_5L_2L_3 + a_6L_3L_1. \tag{2.29}$$

In order to determine the coefficients $a_1, \ldots, a_6$, six constrained conditions are required. Here we make use of the following constraints: three PVs at the vertexes, one VIA over the cell and the first order derivatives d_{xi}, d_{yi} for x, y-directions at the middle point of the cell element. As will be shown later, the first order derivatives d_{xi} and d_{yi} are not treated as a prognostic variables, but approximated by other moments in a manner of the CIP-CSL3 scheme [38].

We summarize the constrained conditions as,

$$\begin{cases} \mathcal{Q}_i(1,0,0) = a_1 = \overline{P_v q}_{i1}, \\ \mathcal{Q}_i(0,1,0) = a_2 = \overline{P_v q}_{i2}, \\ \mathcal{Q}_i(0,0,1) = a_3 = \overline{P_v q}_{i3}, \\ \int_{s_i} \mathcal{Q}_i(L_1, L_2, L_3)ds = \frac{1}{3}(a_1 + a_2 + a_3) + \frac{1}{12}(a_4 + a_5 + a_6) = \overline{V q}_i, \\ \frac{\partial \mathcal{Q}_i}{\partial x}\left(\frac{1}{3},\frac{1}{3},\frac{1}{3}\right) = \frac{y_{i2}-y_{i3}}{J_i}\frac{\partial \mathcal{Q}_i}{\partial L_1} + \frac{y_{i3}-y_{i1}}{J_i}\frac{\partial \mathcal{Q}_i}{\partial L_2} + \frac{y_{i1}-y_{i2}}{J_i}\frac{\partial \mathcal{Q}_i}{\partial L_3} = d_{xi}, \\ \frac{\partial \mathcal{Q}_i}{\partial y}\left(\frac{1}{3},\frac{1}{3},\frac{1}{3}\right) = \frac{x_{i3}-x_{i2}}{J_i}\frac{\partial \mathcal{Q}_i}{\partial L_1} + \frac{x_{i1}-x_{i3}}{J_i}\frac{\partial \mathcal{Q}_i}{\partial L_2} + \frac{x_{i2}-x_{i1}}{J_i}\frac{\partial \mathcal{Q}_i}{\partial L_3} = d_{yi}. \end{cases} \tag{2.30}$$

The gradients in terms of L_1, L_2, L_3 at cell center are

$$\begin{aligned} \frac{\partial \mathcal{Q}_i}{\partial L_1}\left(\frac{1}{3},\frac{1}{3},\frac{1}{3}\right) &= a_1 + \frac{1}{3}(a_4 + a_6), \\ \frac{\partial \mathcal{Q}_i}{\partial L_2}\left(\frac{1}{3},\frac{1}{3},\frac{1}{3}\right) &= a_2 + \frac{1}{3}(a_4 + a_5), \\ \frac{\partial \mathcal{Q}_i}{\partial L_3}\left(\frac{1}{3},\frac{1}{3},\frac{1}{3}\right) &= a_3 + \frac{1}{3}(a_5 + a_6). \end{aligned} \tag{2.31}$$

From 2.30, 2.27 and 2.31, the coefficients $a_1, \ldots, a_6$ are determined as follows:

$$\begin{aligned} a_1 &= \overline{P_v q}_{i1}, \\ a_2 &= \overline{P_v q}_{i2}, \\ a_3 &= \overline{P_v q}_{i3}, \\ a_4 &= 4\overline{V q}_i - \frac{1}{3}\left(7\overline{P_v q}_{i1} + 7\overline{P_v q}_{i2} - 2\overline{P_v q}_{i3}\right) + (x_{i1} + x_{i2} - 2x_{i3})d_{xi} + (y_{i1} + y_{i2} - 2y_{i3})d_{yi}, \\ a_5 &= 4\overline{V q}_i - \frac{1}{3}\left(-2\overline{P_v q}_{i1} + 7\overline{P_v q}_{i2} + 7\overline{P_v q}_{i3}\right) + (-2x_{i1} + x_{i2} + x_{i3})d_{xi} + (-2y_{i1} + y_{i2} + y_{i3})d_{yi}, \\ a_6 &= 4\overline{V q}_i - \frac{1}{3}\left(7\overline{P_v q}_{i1} - 2\overline{P_v q}_{i2} + 7\overline{P_v q}_{i3}\right) + (x_{i1} - 2x_{i2} + x_{i3})d_{xi} + (y_{i1} - 2y_{i2} + y_{i3})d_{yi}. \end{aligned} \tag{2.32}$$

The first order derivatives d_{xi} and d_{yi} for cell i are estimated by using the PVs $(\overline{P_m q}_{ij})$ defined at the middle point of boundary lines through Gauss divergence formula as

$$\begin{aligned} d_{xi} &= \frac{1}{\Delta s_i}\sum_{j=1}^{3} |\Delta l_{ij}|(\overline{P_m q} n_x)_{ij}, \\ d_{yi} &= \frac{1}{\Delta s_i}\sum_{j=1}^{3} |\Delta l_{ij}|(\overline{P_m q} n_y)_{ij}. \end{aligned} \tag{2.33}$$

Given the first order derivatives d_{xi} and d_{yi} for cell i and its three neighbors, the limiting projection to eliminate the numerical oscillation is conducted by modifying the slope parameters d_{xi} and d_{yi} in x and y-directions separately in a manner similar to the 1D case.

Analogous to the 1D case, moments are updated by the following ordinary differential equations,

- PV :

$$\frac{d\overline{P}\overline{q}_{ij}}{dt} = -\left(\partial_x \mathcal{F}_{ij} + \partial_y \mathcal{G}_{ij}\right), \tag{2.34}$$

where $\overline{Pq}_{ij}$ denotes both $\overline{P_v q}_{ij}$ and $\overline{P_m q}_{ij}$ with $j = 1, 2, 3$.

- VIA :

$$\frac{d\overline{V}\overline{q}_i}{dt} = -\frac{1}{\Delta s_i}\int_{s_i}\left(\frac{\partial F(q)}{\partial x} + \frac{\partial G(q)}{\partial y}\right)ds, = -\frac{1}{\Delta s_i}\sum_{j=1}^{3}\int_{l_{ij}}\left(\mathcal{F}_{ij}n_{xij} + \mathcal{G}_{ij}n_{yij}\right)dl. \tag{2.35}$$

The time integration is conducted by the third-order TVD Runge-Kutta method shown before. The point-wise formulation for the numerical flux for PV moment in 1D (2.14) can be straightforwardly extended to 2D. At first, we evaluate the first order derivatives of the state variable q from the piecewise interpolation reconstruction over each triangular mesh element. Since they may be discontinuous at the vertexes v_{ij} as well as the middle points m_{ij} of boundary lines in both x and y-directions, the "left" and "right" values in x-direction are computed by

$$\begin{cases} \partial_x q_{ij}^- = \frac{\partial}{\partial x}\mathcal{Q}^{x^-}(x_{ij}, y_{ij}) & \text{if } x < x_{ij}. \\ \partial_x q_{ij}^+ = \frac{\partial}{\partial x}\mathcal{Q}^{x^+}(x_{ij}, y_{ij}) & \text{if } x > x_{ij}, \end{cases} \tag{2.36}$$

and the "lower" and "upper" values in y-direction are computed by

$$\begin{cases} \partial_y q_{ij}^- = \frac{\partial}{\partial y}\mathcal{Q}^{y^-}(x_{ij}, y_{ij}) & \text{if } y < y_{ij}, \\ \partial_y q_{ij}^+ = \frac{\partial}{\partial y}\mathcal{Q}^{y^+}(x_{ij}, y_{ij}) & \text{if } y > y_{ij}. \end{cases} \tag{2.37}$$

Here, $\mathcal{Q}^{x^\pm}(x_{ij}, y_{ij})$ denotes the cell-wise interpolation function (2.29) on the cell right or left to point (x_{ij}, y_{ij}), while $\mathcal{Q}^{y^\pm}(x_{ij}, y_{ij})$ the cell-wise interpolation function on the cell upper or lower to point (x_{ij}, y_{ij}). The derivatives of interpolation function $\mathcal{Q}$ in respect to x and y in (2.36) and 2.37) are obtained in terms of the local area coordinate by (2.28).

We make use of the following LLF approximate Riemann solver to compute the numerical derivatives of fluxes $\partial_x \mathcal{F}$ and $\partial_y \mathcal{G}$

$$\begin{aligned} \partial_x \mathcal{F}_{ij} &= \frac{1}{2}\left\{\partial_x F\left(\partial_x q_{ij}^-\right) + \partial_x F\left(\partial_x q_{ij}^+\right) - \alpha_{ij}\left(\partial_x q_{ij}^+ - \partial_x q_{ij}^-\right)\right\}, \\ \partial_y \mathcal{G}_{ij} &= \frac{1}{2}\left\{\partial_y G\left(\partial_y q_{ij}^-\right) + \partial_y G\left(\partial_y q_{ij}^+\right) - \beta_{ij}\left(\partial_y q_{ij}^+ - \partial_y q_{ij}^-\right)\right\}, \end{aligned} \tag{2.38}$$

where $\partial_x F(\partial_x q_{ij}^\pm)$ and $\partial_y G(\partial_y q_{ij}^\pm)$ are the first order derivatives of flux functions computed from $\partial_x q_{ij}^\pm$ and $\partial_y q_{ij}^\pm$. $\alpha_{ij} = |\partial F/\partial q|_{ij}$ and $\beta_{ij} = |\partial G/\partial q|_{ij}$ are the largest characteristic velocity in x and y-directions, respectively.

The numerical fluxes required for updating VIA in (2.35) is computed by using the PVs on the cell surface readily obtained by (2.34). In the present paper a 3-point quadrature is implemented along each boundary line segment. Provided a line segment l_{ij} having its two ends located at P_1 and P_2 while its central point at P_m, the line integration of a function $\psi(x, y)$ over l_{ij} is computed by the three-point Simpson's formula,

$$\int_{l_{ij}}\psi(x, y)dl \approx \frac{\psi(P_1) + \psi(P_2) + 4\psi(P_m)}{6}|\Delta l_{ij}|. \tag{2.39}$$

3. Formulation for the shallow water equations

In this section, we describe the multi-moment finite volume formulation for the shallow water equations.

3.1. One dimensional case

The one dimensional shallow water equations with topographic source term read

$$\begin{aligned} &\frac{\partial \mathbf{q}}{\partial t} + \frac{\partial \mathbf{F}(\mathbf{q})}{\partial x} = \mathbf{S}, \\ &\mathbf{q} = \begin{bmatrix} h \\ M \end{bmatrix}, \quad \mathbf{F}(\mathbf{q}) = \begin{bmatrix} M \\ \frac{M^2}{h} + \frac{1}{2}gh^2 \end{bmatrix}, \quad \mathbf{S} = \begin{bmatrix} 0 \\ -gh\frac{\partial z}{\partial x} \end{bmatrix}, \end{aligned} \tag{3.1}$$

where $\mathbf{q}$ is the vector of conservative variables, $\mathbf{F}(\mathbf{q})$ the flux function vector and $\mathbf{S}$ the source term of bottom topography. Furthermore, h is the water depth, u the velocity, $M = hu$ the momentum (or discharge), g the gravitational acceleration

and z the elevation of the bottom. In addition, we define the total height $H = h + z$ for use in the formulation dealing with bottom topography, which will be discussed later.

The Jacobian matrix $\mathbf{A}$ for the flux is defined as follows:

$$\mathbf{A} \equiv \frac{\partial \mathbf{F}(\mathbf{q})}{\partial \mathbf{q}} = \begin{bmatrix} 0 & 1 \\ c^2 - u^2 & 2u \end{bmatrix}, \tag{3.2}$$

where $c(=\sqrt{gh})$ is the speed of the gravitational wave and $u(=M/h)$ is the velocity of fluid. It is easy to find the eigenvalues $\lambda^{1,2}$ of $\mathbf{A}$ and the corresponding eigenvectors $r^{1,2}$ as

$$\lambda^1 = u - c, \quad \lambda^2 = u + c, \quad r^1 = \begin{bmatrix} 1 \\ u - c \end{bmatrix}, \quad r^2 = \begin{bmatrix} 1 \\ u + c \end{bmatrix}. \tag{3.3}$$

For the static condition ($h + z = H = \text{const.}$, $M = 0$), it is not trivial to get the balance between the numerical flux and the source term, known also as the "C-property" [4,40,24,41]. One needs to consider the balance in the momentum equation, i.e.

$$\frac{\partial}{\partial x}\left(\frac{1}{2}gh^2\right) = -gh\frac{\partial z}{\partial x}. \tag{3.4}$$

If a formulation does not preserve this balance between the source term and the flux gradient at the discrete level, it may result in spurious oscillations. As we can see from (3.10) given immediately, the PV moments computed by a point-wise approximate Riemann solver automatically satisfy the C-property even if we use the flux functions and the source terms given in (3.1).

When computing the VIA moments by the finite volume formulation, however, we need to recast the flux and source terms in the following equivalent form using the total height H

$$\mathbf{F}(\mathbf{q}) = \begin{bmatrix} M \\ \frac{M^2}{h} + \frac{1}{2}gH^2 \end{bmatrix}, \quad \mathbf{S} = \begin{bmatrix} 0 \\ gz\frac{\partial H}{\partial x} \end{bmatrix}, \tag{3.5}$$

where the geopotential height is expressed in H rather than h. It is clear that under the static condition the source and the flux term will cancel out, thus the C-property is satisfied.

For shallow water equations, the VIA and PV moments of $\mathbf{q}$ and H are defined as follows:

- VIA :

$$\overline{{}^{V}\mathbf{q}}_i \equiv \frac{1}{\Delta x_i}\int_{x_{i-\frac{1}{2}}}^{x_{i+\frac{1}{2}}} \mathbf{q}(x,t)dx, \quad \overline{{}^{V}H}_i = \overline{{}^{V}h}_i + \overline{{}^{V}z}_i, \tag{3.6}$$

- PV :

$$\overline{{}^{P}\mathbf{q}}_{i+\frac{1}{2}} \equiv \mathbf{q}(x_{i+\frac{1}{2}}, t), \quad \overline{{}^{P}H}_{i+\frac{1}{2}} = \overline{{}^{P}h}_{i+\frac{1}{2}} + z_{i+\frac{1}{2}}. \tag{3.7}$$

For a given topography $z_x = \frac{\partial z}{\partial x}$, the PV moment is updated by applying the LLF Riemann solver to the derivative of the hyperbolic flux function $\mathbf{F}$ in (3.1),

$$\begin{aligned}
\frac{d\overline{{}^{P}\mathbf{q}}_{i+\frac{1}{2}}}{dt} &= -\partial_x \mathcal{F}_{i+1/2} + \mathcal{S}_{i+1/2} \\
&= -\frac{1}{2}\left\{ \begin{bmatrix} M_x^+ \\ 2uM_x^+ - u^2h_x^+ + c^2h_x^+ \end{bmatrix}_{i+\frac{1}{2}} + \begin{bmatrix} M_x^- \\ 2uM_x^- - u^2h_x^- + c^2h_x^- \end{bmatrix}_{i+\frac{1}{2}} - \alpha_{i+\frac{1}{2}}\left(\begin{bmatrix} h_x^+ \\ M_x^+ \end{bmatrix}_{i+\frac{1}{2}} - \begin{bmatrix} h_x^- \\ M_x^- \end{bmatrix}_{i+\frac{1}{2}} \right) \right\} \\
&\quad - \begin{bmatrix} 0 \\ \frac{1}{2}c^2 z_{xi+\frac{1}{2}} \end{bmatrix} \\
&= -\frac{1}{2}\left\{ \begin{bmatrix} M_x^+ \\ 2uM_x^+ - u^2h_x^+ + c^2H_x^+ \end{bmatrix}_{i+\frac{1}{2}} + \begin{bmatrix} M_x^- \\ 2uM_x^- - u^2h_x^- + c^2H_x^- \end{bmatrix}_{i+\frac{1}{2}} - \alpha_{i+\frac{1}{2}}\left(\begin{bmatrix} h_x^+ \\ M_x^+ \end{bmatrix}_{i+\frac{1}{2}} - \begin{bmatrix} h_x^- \\ M_x^- \end{bmatrix}_{i+\frac{1}{2}} \right) \right\} \\
&= -\frac{1}{2}\left\{ \partial_x \mathbf{F}'^{+} + \partial_x \mathbf{F}'^{-} - \alpha_{i+\frac{1}{2}}\left(\partial_x \mathbf{q}_{i+\frac{1}{2}}^{+} - \partial_x \mathbf{q}_{i+\frac{1}{2}}^{-} \right) \right\}.
\end{aligned} \tag{3.8}$$

In above rearrangement, we have used the fact that the PVs of the physical variables at cell boundary $x_{i+\frac{1}{2}}$ is continuous. Their gradients $\partial_x \mathbf{q}_{xi+1/2}^{\pm} = [h_{xi+1/2}^{\pm}, M_{xi+1/2}^{\pm}]^T$ and $H_{xi+1/2}^{\pm} = h_{xi+1/2}^{\pm} + z_{xi+\frac{1}{2}}$, on the other hand, are obtained from the interpolation functions in the neighboring cells by (2.13). Here, the largest characteristic velocity $\alpha_{i+\frac{1}{2}}$ is computed by

$$\alpha_{i+\frac{1}{2}} = \max(|\lambda_{i+\frac{1}{2}}^1|, |\lambda_{i+\frac{1}{2}}^2|) = |u_{i+\frac{1}{2}}| + c_{i+\frac{1}{2}}. \tag{3.9}$$

In practice, the effective flux functions in the presence of the topographic effect, $\partial_x \mathbf{F}'$ in (3.8), are computed by,

$$\partial_x \mathbf{F}'^{\pm} = \begin{bmatrix} M_x^{\pm} \\ 2uM_x^{\pm} - u^2 h_x^{\pm} + c^2 H_x^{\pm} \end{bmatrix}. \tag{3.10}$$

It is obvious that $\partial_x \mathbf{F}'$ vanishes under the static condition ($M_x = 0,\ H_x = 0,\ u = 0$), thus the numerical formulation satisfies the C-property.

VIA is computed by the following flux-form equations with the flux functions and source terms given by (3.5),

$$\frac{d^{\overline{V}}\overline{\mathbf{q}}_i}{dt} = -\frac{1}{\Delta x_i}\left(\mathcal{F}_{i+\frac{1}{2}} - \mathcal{F}_{i-\frac{1}{2}}\right) + \frac{1}{\Delta x_i}\int_{x_{i-1/2}}^{x_{i+1/2}} \mathbf{S}\, dx. \tag{3.11}$$

The numerical flux $\mathcal{F}$ is directly estimated by the PVs defined at cell boundaries, and the integration of the topographic source term $gz(\partial H)/(\partial x)$ is computed by a three-point Simpson's quadrature formula.

As discussed previously, we make use of the flux and topographic source term given by (3.5) to ensure the C-property in (3.11). It is obvious that the reconstruction function satisfies $\frac{\partial H}{\partial x} = 0$ everywhere in the static case.

3.2. Two dimensional case

The two dimensional shallow water equations can be written as follows:

$$\frac{\partial \mathbf{q}}{\partial t} + \frac{\partial \mathbf{F}(\mathbf{q})}{\partial x} + \frac{\partial \mathbf{G}(\mathbf{q})}{\partial y} = \mathbf{S}, \tag{3.12}$$

$$\mathbf{q} = \begin{bmatrix} h \\ M \\ N \end{bmatrix}, \quad \mathbf{F}(\mathbf{q}) = \begin{bmatrix} M \\ \frac{M^2}{h} + \frac{1}{2}gh^2 \\ \frac{MN}{h} \end{bmatrix}, \quad \mathbf{G}(\mathbf{q}) = \begin{bmatrix} N \\ \frac{MN}{h} \\ \frac{N^2}{h} + \frac{1}{2}gh^2 \end{bmatrix}, \tag{3.13}$$

where $M = hu,\ N = hv$ are the x and y components of momentum, respectively. The topographic source terms read

$$\mathbf{S} = \begin{bmatrix} 0 \\ -gh\frac{\partial z}{\partial x} \\ -gh\frac{\partial z}{\partial y} \end{bmatrix}. \tag{3.14}$$

The Jacobian matrices are written as follows:

$$\mathbf{A} \equiv \frac{\partial \mathbf{F}(\mathbf{q})}{\partial \mathbf{q}} = \begin{bmatrix} 0 & 1 & 0 \\ c^2 - u^2 & 2u & 0 \\ -uv & v & u \end{bmatrix}, \quad \mathbf{B} \equiv \frac{\partial \mathbf{G}(\mathbf{q})}{\partial \mathbf{q}} = \begin{bmatrix} 0 & 0 & 1 \\ -uv & v & u \\ c^2 - v^2 & 0 & 2v \end{bmatrix}. \tag{3.15}$$

The eigenvalue $\lambda^{1,2,3}$ of $\mathbf{A}$ and the corresponding eigenvector $r^{1,2,3}$ read,

$$\lambda^1 = u - c, \quad \lambda^2 = u, \quad \lambda^3 = u + c, \tag{3.16}$$

$$r^1 = \begin{bmatrix} 1 \\ u - c \\ v \end{bmatrix}, \quad r^2 = \begin{bmatrix} 0 \\ 0 \\ 1 \end{bmatrix}, \quad r^3 = \begin{bmatrix} 1 \\ u + c \\ v \end{bmatrix}, \tag{3.17}$$

while the eigenvalue $\lambda^{1,2,3}$ of $\mathbf{B}$ and the corresponding eigenvector $r^{1,2,3}$ read,

$$\lambda^1 = v - c, \quad \lambda^2 = v, \quad \lambda^3 = v + c, \tag{3.18}$$

$$r^1 = \begin{bmatrix} 1 \\ u \\ v - c \end{bmatrix}, \quad r^2 = \begin{bmatrix} 0 \\ 1 \\ 0 \end{bmatrix}, \quad r^3 = \begin{bmatrix} 1 \\ u \\ v + c \end{bmatrix}. \tag{3.19}$$

In analog to the 1D case, PVs are computed by the following evolution equations

$$\frac{d^{\overline{P}}\overline{\mathbf{q}}_{ij}}{dt} = -\left(\partial_x \mathcal{F}_{ij} + \partial_y \mathcal{G}_{ij}\right) + \mathcal{S}_{ij}. \tag{3.20}$$

The hyperbolic part of the numerical fluxes are computed by the approximate LLF Riemann solver. After the manipulations similar to 1D, we have

$$\frac{d^{\overline{P}}\overline{\mathbf{q}}_{ij}}{dt} = -\frac{1}{2}\left\{\partial_x \mathbf{F}'^{-} + \partial_x \mathbf{F}'^{+} - \alpha_{ij}\left(\partial_x \mathbf{q}_{ij}^{+} - \partial_x \mathbf{q}_{ij}^{-}\right)\right\} - \frac{1}{2}\left\{\partial_y \mathbf{G}'^{-} + \partial_y \mathbf{G}'^{+} - \beta_{ij}\left(\partial_y \mathbf{q}_{ij}^{+} - \partial_y \mathbf{q}_{ij}^{-}\right)\right\}, \tag{3.21}$$

where α and β stand for the largest eigenvalues of **A** and **B**, respectively, and

$$\begin{aligned}\partial_x \mathbf{F}'^{\pm} &= \begin{bmatrix} M_x^{\pm} \\ 2uM_x^{\pm} - u^2 h_x^{\pm} + c^2 H_x^{\pm} \\ -uvh_x^{\pm} + vM_x^{\pm} + uN_x^{\pm} \end{bmatrix}, \\ \partial_y \mathbf{G}'^{\pm} &= \begin{bmatrix} N_y^{\pm} \\ -uvh_y^{\pm} + vM_y^{\pm} + uN_y^{\pm} \\ 2vN_y^{\pm} - v^2 h_y^{\pm} + c^2 H_y^{\pm} \end{bmatrix}. \end{aligned} \tag{3.22}$$

VIA is updated by a finite volume formulation. Again, similar to (3.5), we re-write the numerical flux and the topographic source terms in the total height of the water surface $H = h + z$ as,

$$\mathbf{F}(\mathbf{q}) = \begin{bmatrix} M \\ \frac{M^2}{h} + \frac{1}{2} g H^2 \\ \frac{MN}{h} \end{bmatrix}, \quad \mathbf{G}(\mathbf{q}) = \begin{bmatrix} N \\ \frac{MN}{h} \\ \frac{N^2}{h} + \frac{1}{2} g H^2 \end{bmatrix} \quad \text{and} \quad \mathbf{S} = \begin{bmatrix} 0 \\ gz \frac{\partial H}{\partial x} \\ gz \frac{\partial H}{\partial y} \end{bmatrix}. \tag{3.23}$$

The finite volume formulation to update the VIA moment reads

$$\frac{d\overline{\mathbf{q}}_i}{dt} = -\frac{1}{\Delta s_i} \sum_{j=1}^{3} \int_{l_{ij}} (\mathcal{F}_{ij} n_{xij} + \mathcal{G}_{ij} n_{yij}) dl + \frac{1}{\Delta s_i} \int_{s_i} \mathbf{S} ds, \tag{3.24}$$

where a three-point Simpson's formula (2.39) is used to compute the line integration of the flux functions over each boundary segment, and area integration of source term is calculated by a seven-point integration formula using the six point values along the cell boundary (i.e. three at the triangle vertices and three at the middle points of the three line segments) and one at the cell center. It is obvious that with (3.23) expressing the flux functions and the source terms in the total height H, finite volume formulation (3.24) satisfies the C-property.

4. Numerical results

In this section, we present the numerical results of some typical test problems for the one and two dimensional shallow water equations. Without further explanation, we use the SI unit system for all variables. The gravity constant is 9.8 m/s^2.

4.1. One dimensional numerical tests

4.1.1. Dam-break flow

In the first numerical test, dam-break is solved in a domain of [0,200]. The mesh number is 200 with uniform spacing $\Delta x = 1$. The initial conditions are

$$\begin{aligned} h_0(x) &= \begin{cases} h_L & 0.0 \leqslant x \leqslant 100.0, \\ h_R & 100.0 < x \leqslant 200.0, \end{cases} \\ M_0(x) &= 0.0. \end{aligned} \tag{4.1}$$

Two ratios of the initial water depths are separately specified as $h_L/h_R = 10$ (mild shock) and $h_L/h_R = 100$ (strong shock). In both cases, a right-moving shock wave and a left-expanding rarefaction fan are generated after the instantaneous collapse of the dam. The exact solution is available in [30]. From numerical experiments, we find that the maximum CFL number $((|u| + c)\Delta t/\Delta x)$ allowable for computational stability is around 0.41. We used a CFL number of 0.1 in this test, and computed the numerical solutions until $t = 20.0$.

The simulated water depth h and the velocity u are depicted against the exact solutions in Figs. 4 and 5. Both the shock wave and the rarefaction wave are accurately resolved. The conservation of the VIA quantities guarantees the correct location of the shock wave. The CIP-CSL3 reconstruction with the slope parameter given by (2.7) eliminates the spurious oscillation and the numerical diffusion is also effectively controlled.

4.1.2. Symmetrical rarefaction waves

As given in [30], a symmetrically diverging velocity creates two strong rarefaction waves traveling in opposite directions. The initial condition is given by

$$\begin{aligned} h_0(x) &= 1.0, \\ M_0(x) &= \begin{cases} -5.0 & 0.0 \leqslant x \leqslant 25.0, \\ 5.0 & 25.0 < x \leqslant 50.0. \end{cases} \end{aligned} \tag{4.2}$$

The mesh number is 200 and the CFL number is 0.1. As commentated in [30], this test results in a very thin water layer in the domain center that may cause a negative height in the numerical outputs of some schemes. The numerical solutions of the water depth h, and the velocity u at $t = 2.5$ are plotted in Fig. 6. The thin wet bed is accurately captured.

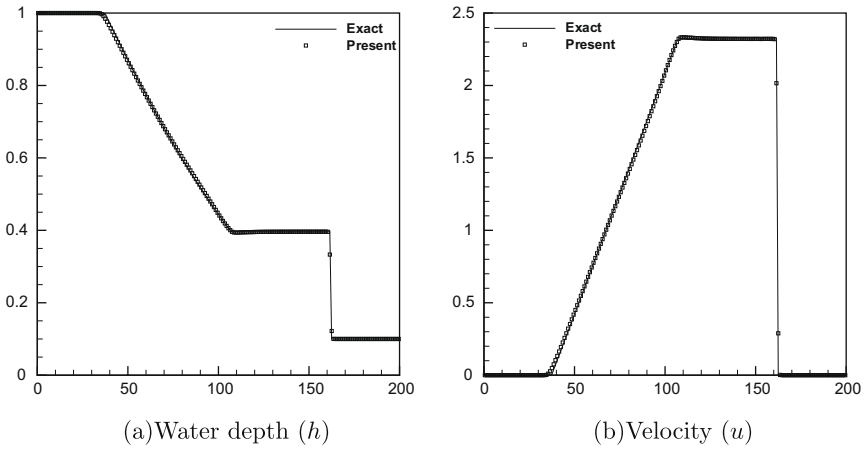

Fig. 4. Numerical results (mild shock) of water depth (a) and velocity (b) at $t = 20.0$ by the present method (circles) and the exact solution (solid line).

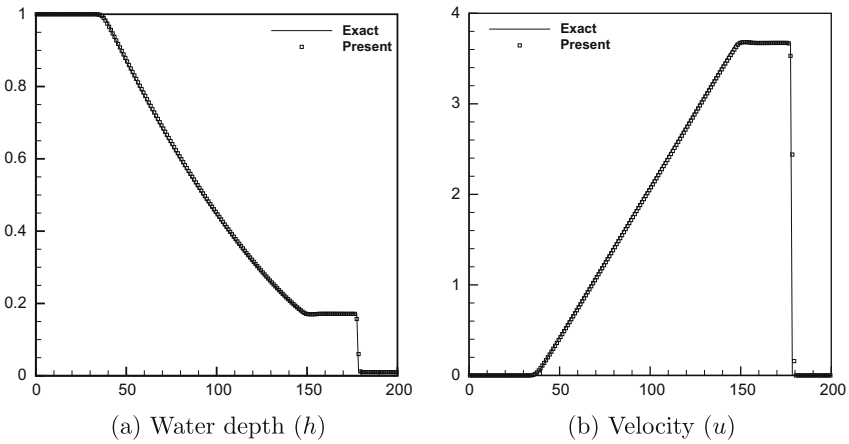

Fig. 5. Same as Fig. 4, but for the strong shock case.

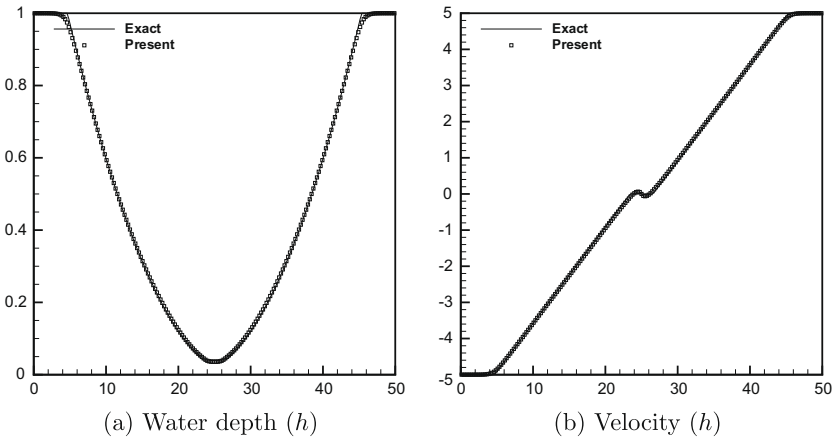

Fig. 6. Numerical results of water depth (a) and velocity (b) at $t = 2.5$ by the present method (circles) and the exact solution (solid line).

4.1.3. Evaluation of the exact C-property

The purpose of this test [40,41] is to verify the exact C-property of the formulation over a non-flat bottom. In this paper, we computed with two different profiles of the bottom topography separately given by

$$z(x) = 5.0 \exp\left(-\frac{2}{5}(x-5.0)^2\right), \tag{4.3}$$

and

$$z(x) = \begin{cases} 4.0 & \text{if } 4.0 \leqslant x \leqslant 8.0, \\ 0.0 & \text{otherwise.} \end{cases} \tag{4.4}$$

It is clear that (4.3) gives a smooth bottom and (4.4) a discontinuous one. The initial conditions are specified as a stationary state,

$$H_0(x) = h_0(x) + z(x) = 10.0, \quad M_0(x) = 0.0, \tag{4.5}$$

which should be exactly maintained physically.

We used a mesh of 200 cells and computed the solutions until $t = 0.5$ with the CFL number of 0.1. The L^1 errors for the water height h and the discharge $M = hu$ are given in Table 1 for the two bottom profiles. It is observed that the L^1 errors in both PV and VIA moments are of a magnitude within the round-off error, which manifests the exact C-property of the proposed numerical method.

4.1.4. Perturbation of a lake at rest

The purpose of this example is to test the present formulation for source term in the case of a small perturbation of a lake at rest with variable bottom topography. The bottom topography is given by

$$z(x) = \begin{cases} 0.25(1.0 + \cos(10.0\pi(x-0.5))) & \text{if } 1.4 \leqslant x \leqslant 1.6, \\ 0.0 & \text{otherwise,} \end{cases} \tag{4.6}$$

over the computational domain [0,2]. The initial conditions are

$$\begin{aligned} H_0(x) &= \begin{cases} 1.0 + \Delta H & \text{if } 1.1 \leqslant x \leqslant 1.2, \\ 1.0 & \text{otherwise,} \end{cases} \\ M_0(x) &= 0.0. \end{aligned} \tag{4.7}$$

where ΔH is a non-zero perturbation constant. Two cases with the initial perturbations respectively being $\Delta H = 0.2$ (big pulse) and $\Delta H = 0.001$ (small pulse) have been examined. The solutions at $t = 0.2$ for the big pulse $\Delta H = 0.2$ over 201 mesh cells and 3001 mesh cells are shown in Fig. 7. The results for small pulse $\Delta H = 0.001$ are shown in Fig. 8. The numerical re-

Table 1
L^1 errors for the stationary solution with a smooth bottom (4.3) and a discontinuous bottom (4.4).

Bottom	L^1 error in PV		L^1 error in VIA	
	H	M	H	M
Smooth	7.47E−14	2.48E−13	7.37E−14	2.47E−13
Discontinuous	6.80E−15	4.16E−14	6.33E−15	4.15E−14

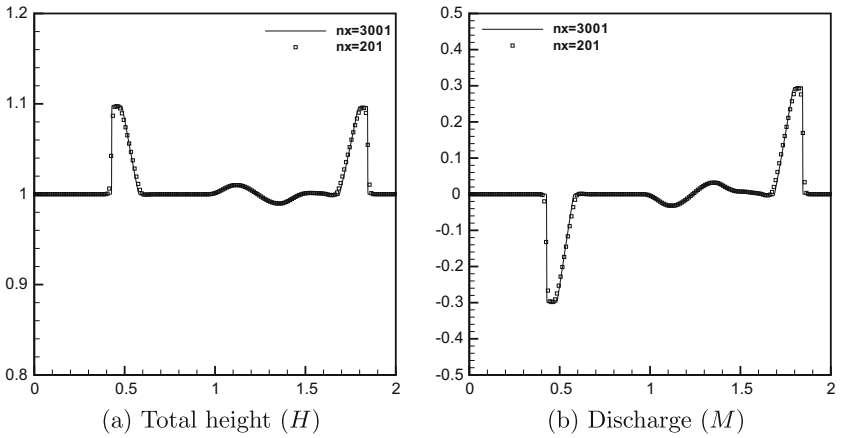

Fig. 7. Numerical results (big pulse) of total height (a) and discharge (b) at $t = 0.2$ by the present method with a 201 mesh (circle) and a 3001 mesh (solid line).

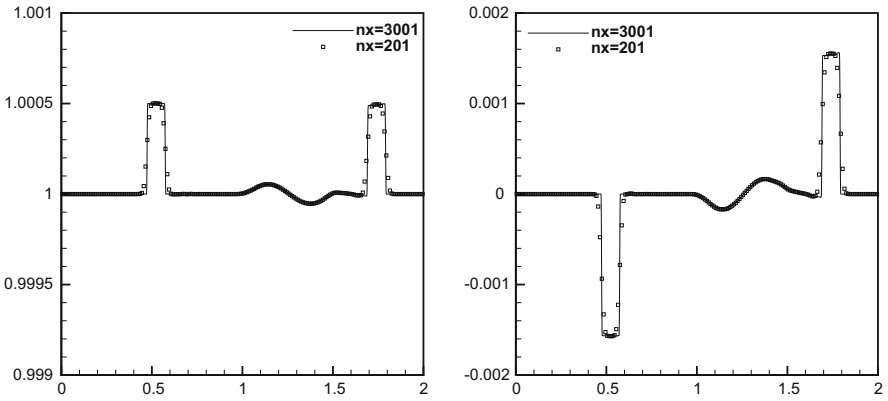

(a) Total height (H) (b) Discharge (M)

Fig. 8. Same as Fig. 7, but for the small pulse case.

sults are accurate and free of spurious oscillations, and look very comparable to those found in other existing literature [22,40,25,41].

4.1.5. Dam-breaking problem over a rectangular bump

We computed the dam-breaking problem over a rectangular bump involving a rapidly varying flow over discontinuous bottom topography. It presents a more serious test for evaluating the robustness and accuracy of the numerical treatment of the source term.

The computational domain is [0,1500], and the bottom topography is given by

$$z(x) = \begin{cases} 8.0 & \text{if } |x - 750| \leqslant 1500/8, \\ 0.0 & \text{otherwise.} \end{cases} \tag{4.8}$$

The initial conditions are

$$\begin{aligned} H_0(x) &= \begin{cases} 20.0 & \text{if } x \leqslant 750, \\ 15.0 & \text{otherwise,} \end{cases} \\ M_0(x) &= 0.0. \end{aligned} \tag{4.9}$$

The numerical results obtained with 401 mesh cells and with 4001 mesh cells are shown in Figs. 9 and 10 for different ending time, $t = 15$ and $t = 60$, respectively. The numerical results show that even for completely discontinuous bottom topography our scheme is still able to reproduce well-balanced and accurate numerical solutions.

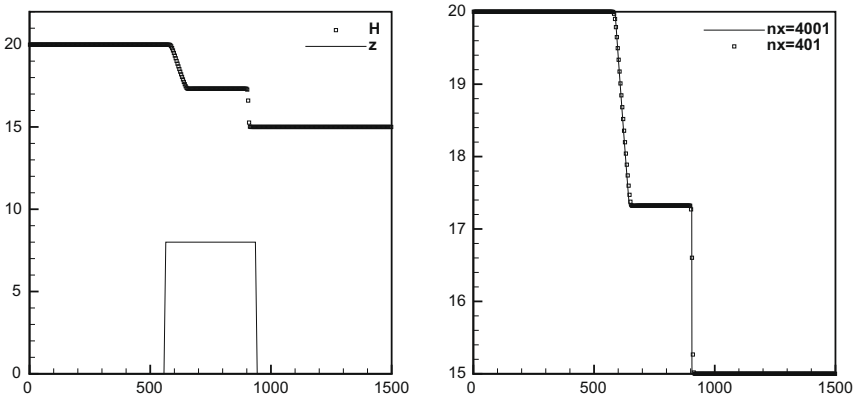

(a) Total height (H) and bottom topography (z) (b) Enlarged view of total height

Fig. 9. Numerical results of total height at $t = 15$. (a) The numerical solution using 401 mesh (circle) with the bottom topography (solid line) and (b) the numerical solutions using a 401 mesh (circle) and a 4001 mesh (solid line).

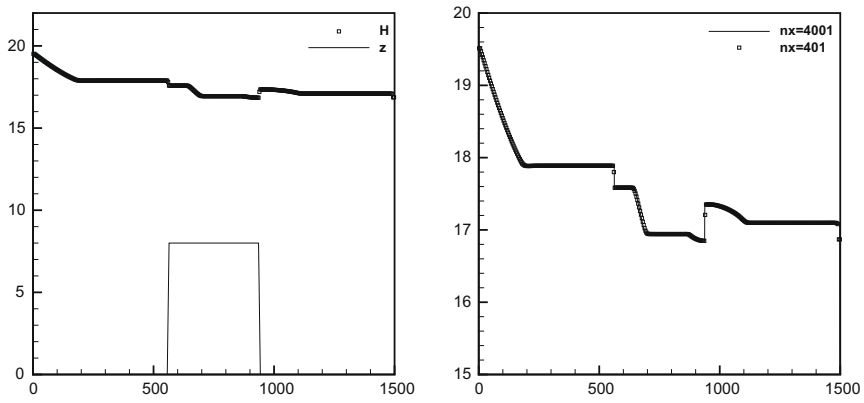

(a) Totalheight (H)and bottom topography(z) (b) Enlarged view of total height

Fig. 10. Same as Fig. 9 but at $t = 60$.

4.1.6. Steady flow over a bump

The 1D shallow water flow over irregular bottom can reach a steady state by controlling the upstream inflow flux and the level of water surface at the outflow end. This type of tests have been used to examine if the numerical solution can converge to the steady state under the effect of bottom topography in literature [14,41,13,31,20,21] as the supplement to the transient flow tests presented before.

Our computational domain is [0,30]. The bottom topography is given by

$$z(x) = \begin{cases} 0.2 - 0.05(x - 10.0)^2 & \text{if } 8 \leqslant x \leqslant 12, \\ 0.0 & \text{otherwise.} \end{cases} \tag{4.10}$$

The initial conditions of a static state is specified by

$$H_0(x) = 0.5, \quad M_0(x) = 0.0. \tag{4.11}$$

Depending on the boundary conditions at the two ends of the domain, different regimes of the final steady state can be obtained. Same as in [32,41], we consider the following three cases by imposing different boundary conditions.

- *Case A:* The discharge $M = 4.42$ is imposed at the left end as the inflow boundary condition, while the water height $h = 2.0$ is imposed at the right end of the domain. These conditions result in a subcritical flow with a shock.
- *Case B:* The discharge $M = 1.53$ is imposed at the left end as the inflow boundary condition, while the water height $h = 0.66$ is imposed downstream only when the flow is subcritical. These conditions result in a transcritical flow without shock.
- *Case C:* The discharge $M = 0.18$ is imposed at the left end as the inflow boundary condition, while the water height $h = 0.33$ is imposed at the right end of the domain. These conditions result in a transcritical flow with a shock.

The computational grid cell number is 200 with uniform size, and the CFL number is =0.1. We computed the three cases until $t = 200$ and plot the numerical results of the total water height ($H = h + z$) and the discharge ($M = hu$) in Figs. 11–13.

The steady solutions of the water height is obtained for all cases with satisfactory accuracy. The discharge solutions, however, have some oscillations as also observed in other methods [14,41,13,31,20,21] with a comparable magnitude. We also observe that the numerical oscillations in the discharge of the steady flows presented here are slightly larger than those in [41]. This can be explained in part by the difference in the limiting projection between the present method and those in [41], which demands to some extent further efforts for better suited limiting in the multi-moment finite volume method.

4.2. Two dimensional numerical tests

In this section, we report five numerical tests of the two dimensional shallow water equations to verify the performance of the proposed model on 2D unstructured grid.

4.2.1. Circular dam-break problem

A two-dimensional circular dam-break [23,33] is solved in the domain of $[0, 200] \times [0, 200]$. The purpose of this problem is to test the ability of the model to preserve the geometrical symmetry of the solution on unstructured mesh. For this purpose, we use an asymmetric mesh as shown in Fig. 14(a) with a mesh number of $100 \times 100 \times 2$.

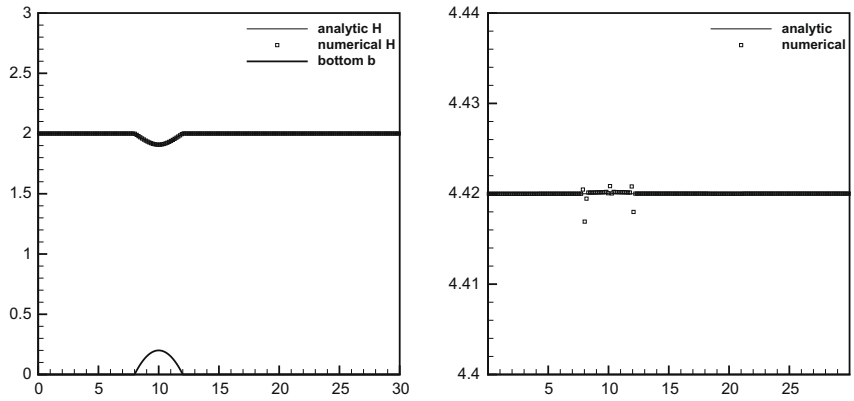

Fig. 11. Steady subcritical flow over a bump. Left: the total water surface height (H), right: the discharge ($M = hu$).

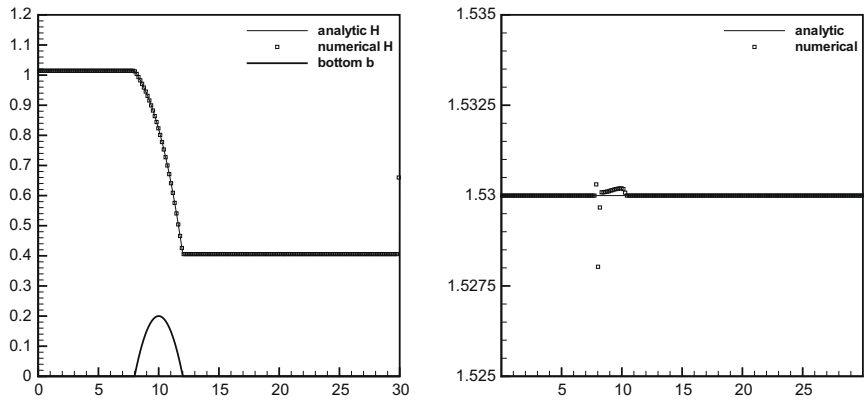

Fig. 12. Steady transcritical flow without shock over a bump. Left: the total water surface height (H), right: the discharge ($M = hu$).

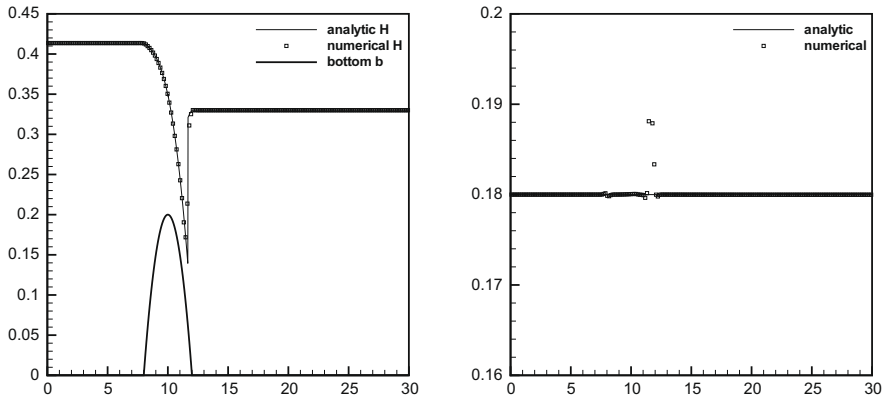

Fig. 13. Steady transcritical flow with a shock over a bump. Left: the total water surface height (H), right: the discharge ($M = hu$).

The initial conditions are

$$h_0(x,y) = \begin{cases} 10.0 & (x-25.0)^2 + (y-25.0)^2 \leqslant (10.5)^2, \\ 1.0 & \text{otherwise}, \end{cases} \qquad (4.12)$$
$$M_0(x,y) = 0.0, \quad N_0(x,y) = 0.0.$$

The CFL number is 0.1. Fig. 15 shows the bird's eye view and contour lines of h at $t = 0.69$. The symmetry of the numerical solution is well preserved. Fig. 16 displays the profiles of h on cross-sections of $x = 0$, $y = 0$ and $y = x$. The semi-analytical

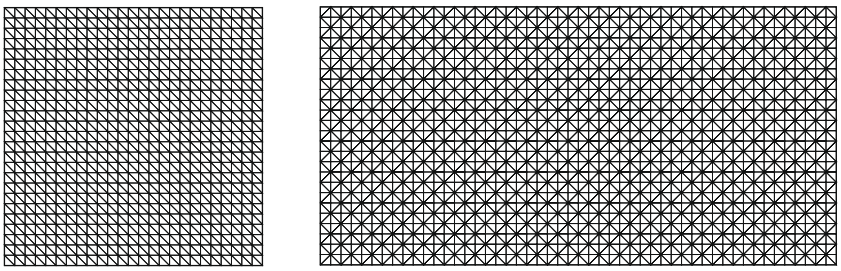

(a) asymmetric mesh (b) symmetric mesh

Fig. 14. Unstructured computational mesh.

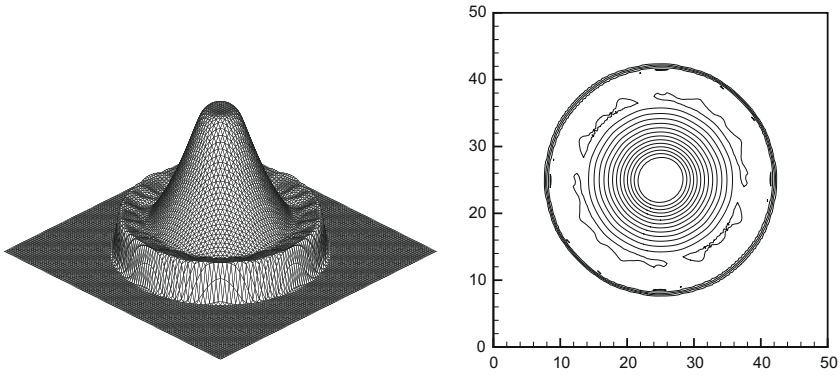

(a) Bird's eye view (b) Contour view

Fig. 15. Numerical results of the circular dam-break at $t = 0.69$. (a) bird's eye view and (b) contour view.

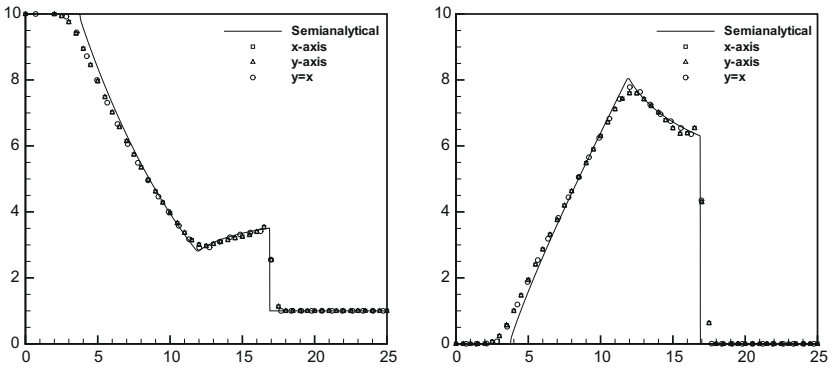

(a) Water depth (h) (b) Velocity ($\sqrt{M^2 + N^2}/h$)

Fig. 16. Numerical results of water depth and velocity at $t = 0.69$ on cross-sections of different orientation against the reference solution (solid line).

solution is obtained by solving the 1D equations in the polar coordinates provided that the solution is exactly axisymmetric [30]. Nearly identical numerical solutions in all directions for shock wave and expansion fan are obtained even on an asymmetric mesh.

4.2.2. Partial dam-break problem

A partial dam-break problem is solved in the domain of $[0, 200] \times [0, 200]$. A dam is located in the middle of the domain and has a 75 wide breach as shown in Fig. 17. The initial conditions are

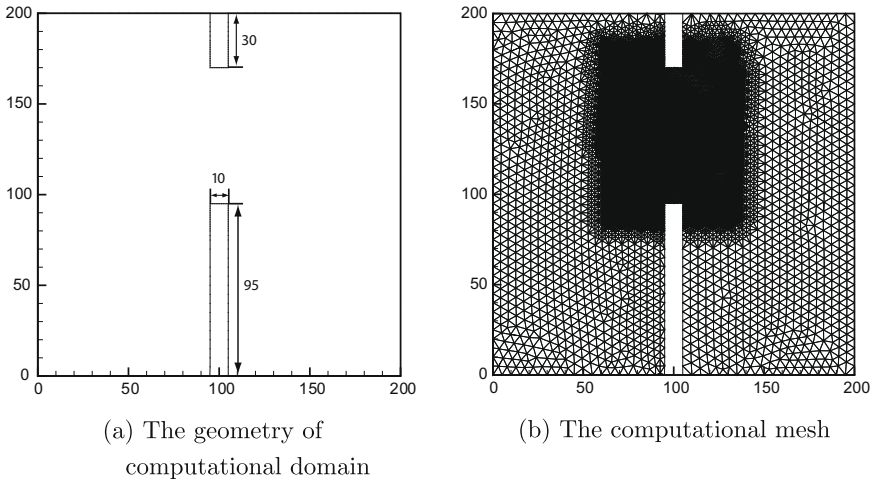

(a) The geometry of computational domain (b) The computational mesh

Fig. 17. Computational conditions of a partially broken dam. (a) Location of dam and (b) computational mesh.

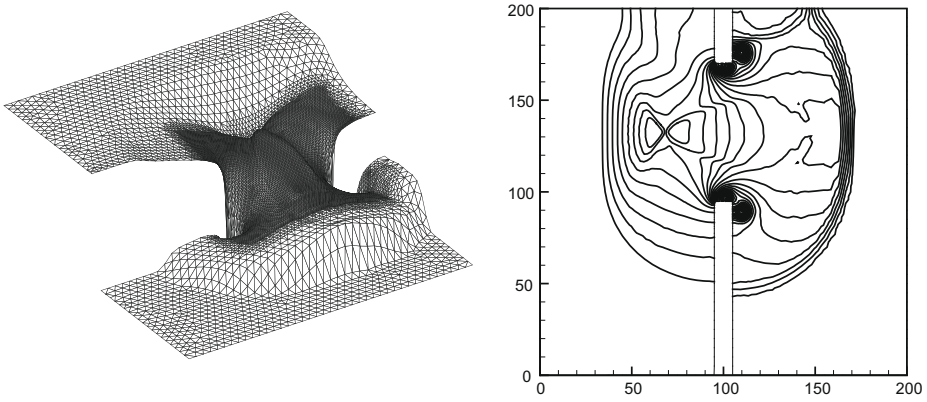

(a) Bird's eye view (b) Contour view

Fig. 18. Numerical results of the water surface at $t = 7.2$. (a) Bird's eye view and (b) contour view (30 contour lines with uniform interval from 2.5 to 9.5).

$$h_0(x,y) = \begin{cases} 10.0 & 0.0 \leqslant x \leqslant 100, \\ 5.0 & 100.0 < x \leqslant 200, \end{cases} \qquad M_0(x,y) = 0.0, \quad N_0(x,y) = 0.0. \tag{4.13}$$

The mesh number is 20,132 and the region close to the breach has finer resolution. The time step is $\Delta t = 0.01$. From above initial condition, a 2D bore wave developed.

Fig. 18 shows the bird's eye view and contour view of h [m] at $t = 7.2$, and Fig. 19 shows the profiles of h, u and v on cross-section of $x = 92.5$. Compared with the reference solutions [11] for this test case, it is found that the present model reproduced the physics with adequate accuracy.

4.2.3. Testing the order of accuracy with the bottom topography

In this test, we examine the convergence rate of the numerical model by computing the 2D nonlinear shallow water equations with bottom topography [40,41]. The elevation of the bottom is given by

$$z(x,y) = \sin(2.0\pi x). \tag{4.14}$$

The initial conditions of the field variables are specified as

$$\begin{aligned} h_0(x,y) &= 10.0 + \exp(\sin(2.0\pi x))\cos(2.0\pi y), \\ M_0(x,y) &= \sin(\cos(2.0\pi x))\sin(2.0\pi y), \\ N_0(x,y) &= \cos(2.0\pi x)\cos(\sin(2.0\pi y)). \end{aligned} \tag{4.15}$$

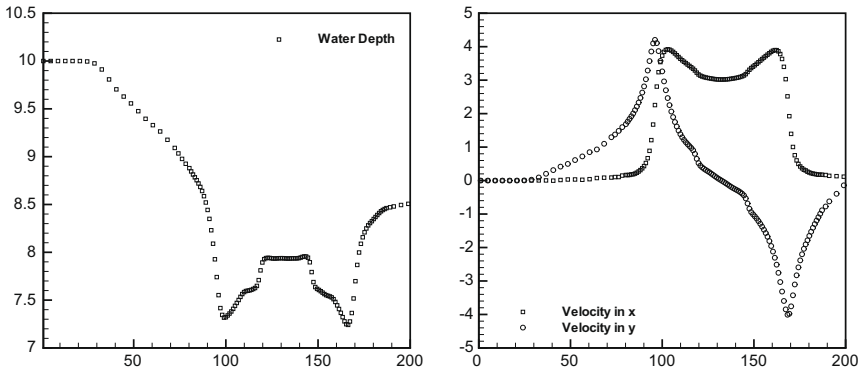

Fig. 19. Numerical results of water depth and velocity at $t = 7.2$ on the cross-section of $x = 92.5$.

The computational domain is $[0,1] \times [0,1]$. The unstructured triangular grid is generated from a Cartesian grid by dividing each of the square element along the diagonal line. A $25 \times 25 \times 2$ mesh, for example, is shown in Fig. 14(a) . Following [40], we stopped the computation at $t = 0.05$ before the development of discontinuous shock solutions. Because the analytical solution is not available for this test, we computed a reference solution with an extremely high resolution ($800 \times 800 \times 2$ grid cells). The numerical outputs from several coarser grids are then compared with the reference solution to get the numerical convergence rates. We give the errors and the convergence rate in Table 2, which justifies a third-order accuracy. The numerical convergence rate is overall higher than those reported in [41] for the DG method.

4.2.4. Two dimensional perturbation with bottom topographic effect

This numerical test is widely used to evaluate numerical schemes for shallow water equations with source terms of bottom topography in 2D [22,40,25,41]. The computational domain is $[0,2] \times [0,1]$, and the bottom topography is given by,

$$z(x,y) = 0.8\exp(-5.0(x-0.9)^2 - 50.0(y-0.5)^2). \tag{4.16}$$

The initial surface level is flat, but a perturbation with a 0.01 jump in height is imposed in the region of $0.05 \leqslant x \leqslant 0.15$. The initial momentum in the x and y-directions are zero.

$$\begin{aligned} H_0(x,y) &= \begin{cases} 1.01 & \text{if } 0.05 \leqslant x \leqslant 0.15, \\ 1.0 & \text{otherwise}, \end{cases} \\ M_0(x,y) &= 0.0, \quad N_0(x,y) = 0.0. \end{aligned} \tag{4.17}$$

The triangular unstructured mesh is similar to Fig. 14(b) but has $200 \times 100 \times 2$ mesh cells. Fig. 20 shows 30 uniformly spaced contour lines of the surface level H at $t = 0.12, 0.24, 0.36, 0.48, 0.60$. The initial perturbation propagates to the right and is affected by the bottom. The reflections and interactions of the surface wave result in complex but symmetrical structures. We include the numerical result computed by the model in [1] on a 400×200 Cartesian mesh as well for comparison. It is observed that the numerical results with triangular grid is in good agreement with the Cartesian structured grid, and the symmetry and the fine flow structures are well resolved.

4.2.5. Solitary Rossby wave

In the final numerical test, we solve the equatorial Rossby soliton analytically studied by Boyd [5], and used to validate numerical models in [12,17] among others. The rotational effect of the Earth is included through the Coriolis force. We use the test set given in [16]. The 2D shallow-water equations of the dimension-less form on the β plane are written as

Table 2
L^1 errors and convergence rate (order of accuracy).

Number of grid cells	H		M		N	
	L^1 error	Order	L^1 error	Order	L^1 error	Order
$25 \times 25 \times 2$	2.28E−03	–	1.10E−02	–	1.91E−02	–
$50 \times 50 \times 2$	3.57E−04	2.67	1.52E−03	2.85	3.03E−03	2.65
$100 \times 100 \times 2$	4.96E−05	2.85	1.93E−04	2.97	4.12E−04	2.88
$200 \times 200 \times 2$	6.37E−06	2.95	2.39E−05	3.02	5.23E−05	2.98

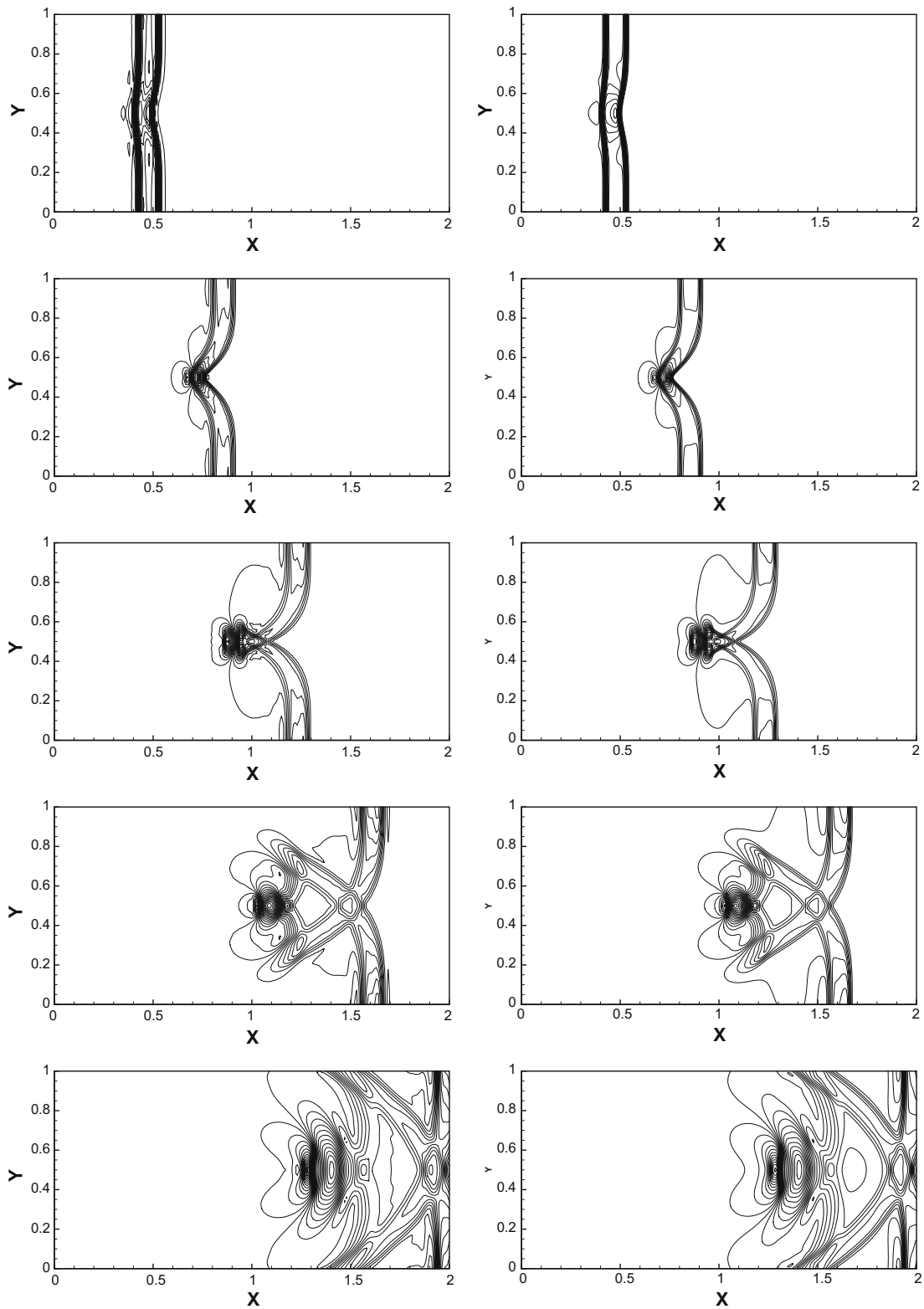

Fig. 20. The contour views of the water surface H. Thirty uniformly spaced contour lines are plotted at instant $t = 0.12, 0.24, 0.36, 0.48$ and 0.6, shown from top to bottom in a time sequence. The minimum and maximum contour lines are 0.99942 and 1.0065 for $t = 0.12$, 0.99318 and 1.01659 for $t = 0.24$, 0.98814 and 1.01161 for $t = 0.36$, 0.99023 and 1.00508 for $t = 0.48$ and 0.99514 to 1.00629 for $t = 0.6$. Left panels: results with a $200 \times 100 \times 2$ triangular unstructured mesh. Right panels: results with a 400×200 Cartesian mesh.

$$\mathbf{q}_t + \mathbf{F}_x(\mathbf{q}) + \mathbf{G}_y(\mathbf{q}) = \mathbf{S},$$
$$\mathbf{q} = \begin{bmatrix} h \\ hu \\ hv \end{bmatrix}, \quad \mathbf{F} = \begin{bmatrix} hu \\ hu^2 + \frac{1}{2}gh^2 \\ huv \end{bmatrix}, \quad \mathbf{G} = \begin{bmatrix} hv \\ huv \\ hv^2 + \frac{1}{2}gh^2 \end{bmatrix}, \quad \mathbf{S} = \begin{bmatrix} 0 \\ f_c hv \\ -f_c hu \end{bmatrix},$$

where the gravity acceleration is set as $g = 1$ and the Coriolis force is computed by the β-plane approximation, $f_c = f_0 + \beta y$ with $f_0 = 0$ and $\beta = 1$, same as those given in [16].

The initial conditions are given by

$$\begin{cases} h_0(x,y) = 1 + \phi(x)\frac{3+6y^2}{4}e^{-0.5y^2}, \\ u_0(x,y) = \phi(x)\frac{-9+6y^2}{4}e^{-0.5y^2}, \\ v_0(x,y) = \phi_x(x)2ye^{-0.5y^2}, \end{cases} \tag{4.18}$$

where, $\phi(x) = 0.771B^2\mathrm{sech}^2(Bx), \phi_x(x) = -2B\phi(x)\tanh(Bx)$, and $B = 0.395$.

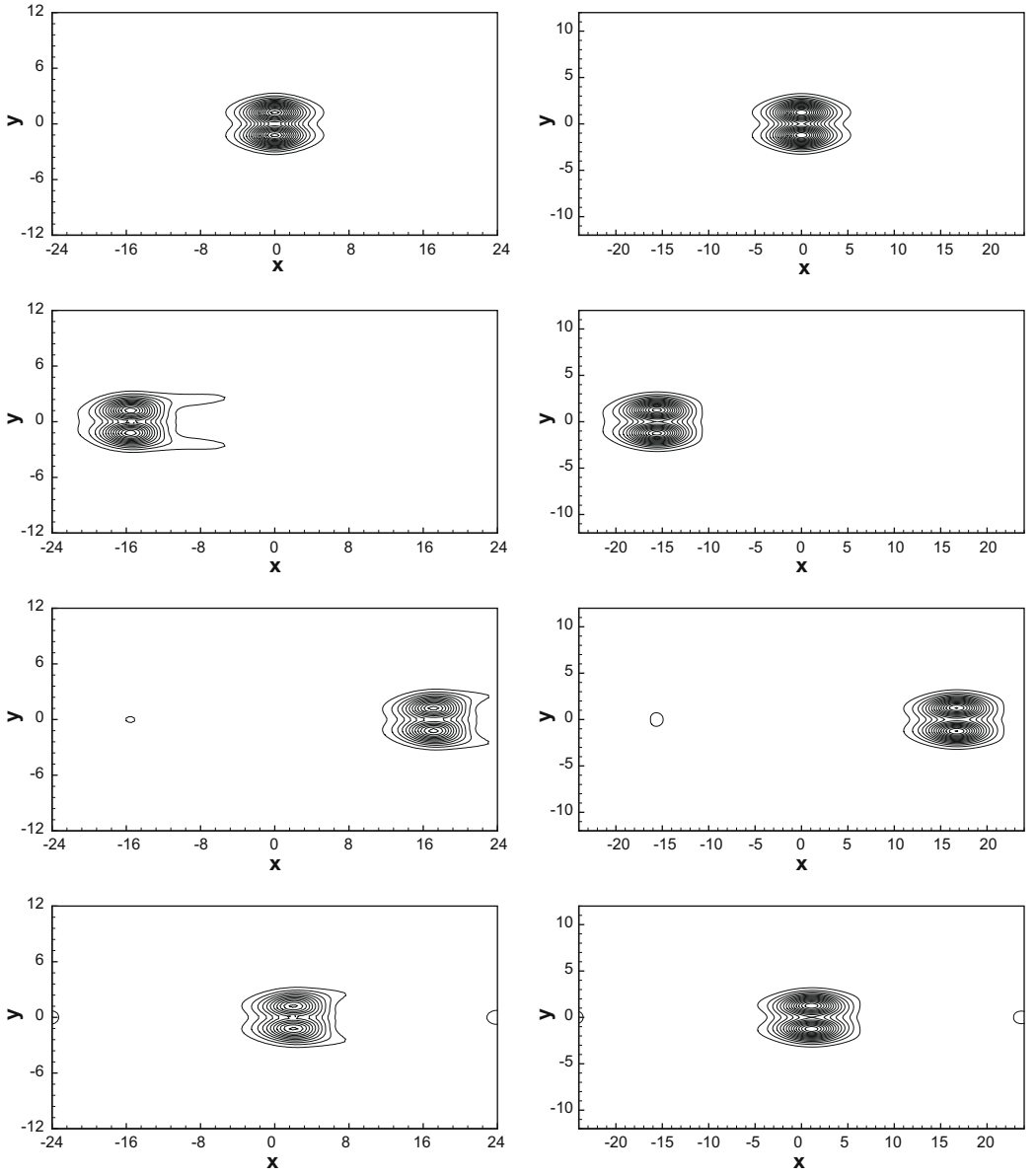

Fig. 21. The contour views of h for Rossby soliton problem at $t = 0, 40, 80, 120$ with 16 uniformly-spaced contour lines from 1.01 to 1.60. Displayed are the numerical results of 2nd-order FV method on a $174 \times 87 \times 2$ mesh (30,276 DOFs) (left), and on a $348 \times 174 \times 2$ mesh (121,104 DOFs) (rights).

The soliton initially defined by (4.18) moves to the left (westward) with a constant phase speed 0.4. The computational domain is set as $[-24, 24] \times [-12, 12]$ and periodical boundary conditions are imposed on left and right ends while the wall conditions are imposed on bottom and top boundaries.

We use two meshes with different resolution to test the present scheme. The coarse mesh has $100 \times 50 \times 2$ cells generated from a Cartesian grid as in Fig. 14(b), while the fine mesh is two level refined by doubling the mesh numbers in x and y directions and has $200 \times 100 \times 2$ cells. With the locally added unknowns, the DOFs of the presented 3rd-order multi-moment finite volume scheme is 30,301 on the coarse mesh, and 120,601 on the fine mesh.

We also include a conventional 2nd-order finite volume scheme for comparison. In the 2nd-order finite volume method, a piece-wise linear interpolation function is constructed with the gradients evaluated by least-square approach using the VIAs on the neighbor cells. Since the VIA is the only unknown on a mesh element in the 2nd-order finite volume method, we use a coarse mesh of $174 \times 87 \times 2$ and a fine mesh of $348 \times 174 \times 2$ for the 2nd-order finite volume model to have the total DOFs of 30,276 and 121,104, respectively being equivalent to those of the multi-moment finite volume model on the coarse and fine meshes.

The computations were run up to $t = 120$ for the soliton to move one period and back to the initial position. The numerical results of the 2nd-order finite volume method with coarse and fine meshes at $t = 0$, 40, 80 and 120 are shown in Fig. 21.

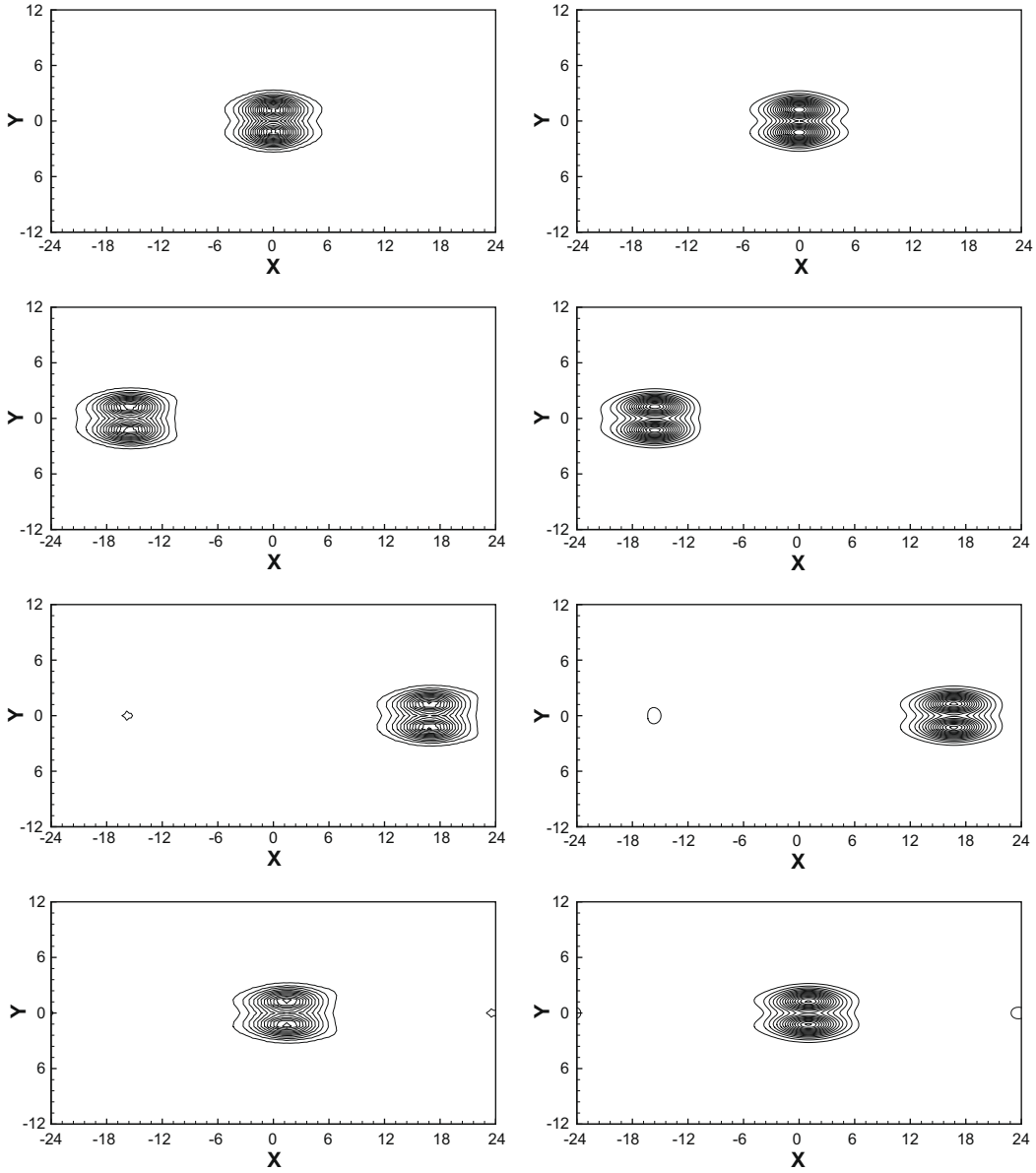

Fig. 22. The contour views of h for Rossby soliton problem at $t = 0, 40, 80, 120$ with 16 uniformly-spaced contour lines from 1.01 to 1.60. Displayed are the numerical results of present method on a $100 \times 50 \times 2$ mesh (30,301 DOFs) (left), and on a $200 \times 100 \times 2$ mesh (120,601 DOFs) (rights).

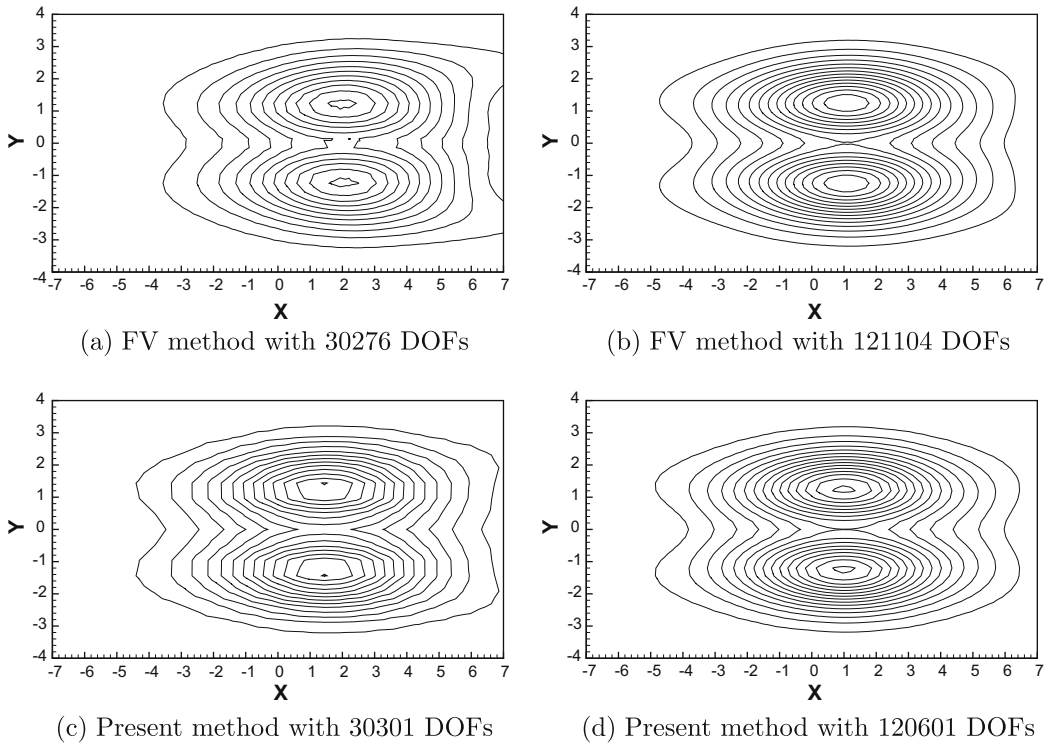

Fig. 23. Enlarged views of the Rossby soliton at $t = 120$.

The results on the coarse mesh suffers serious numerical dissipation and significant lag in the phase speed. The results on the fine mesh are obviously improved.

The numerical results of the present multi-moment finite volume scheme are shown in Fig. 22. In comparison with the 2nd-order finite volume method, the multi-moment finite volume method gives better results with equivalent DOFs. A detailed comparison is done by plotting the enlarged profiles of the solutions at $t = 120$ from different schemes with different mesh resolutions in Fig. 23. The present scheme is more accurate in both phase speed and intensity of the soliton. The maximum value of the height field indicates the numerical dissipation of a scheme. The closer the computed maximum is to the initial value ($\approx$1.169), the more accurate is the numerical solution. The maximum value of the height field at $t = 120$ from the 2nd-order finite volume method is 1.114 on the $174 \times 87 \times 2$ mesh and 1.148 on the $348 \times 174 \times 2$ mesh, while that from the present method is 1.132 on the $100 \times 50 \times 2$ mesh and 1.152 on the $200 \times 100 \times 2$ mesh.

We measured the elapse time of the 2nd-order finite volume method (with a two stage Runge-Kutta time scheme) and that of the multi-moment finite volume method (with a three stage Runge-Kutta time scheme) using same CFL number and DOFs as in this test problem, and found that the multi-moment finite volume model got a 60% increase in the computational time. Considering that one more Runge-Kutta substep is computed in the multi-moment finite volume model, the computational cost increase in the spatial discretization is about 40%.

5. Conclusion

We have constructed an accurate and robust numerical model for shallow water equations on two-dimensional unstructured triangular grid by applying the multi-moment finite volume method.

Two kinds of moments, VIA and PV, are treated as the model variables (unknowns) which are updated by different ways. The PVs are updated by solving point-wisely the local Riemann problems in terms of the derivatives at discrete points on cell boundary, while the VIA moment is updated by the finite volume formulation of flux form, and thus is numerically conserved. The numerical fluxes on the cell boundary required for updating the VIA is computed directly from the point values readily updated as the PV moment, which saves computational cost.

Piecewise parabolic interpolation reconstructions are built by using both VIA and PV moments. The resulting numerical framework has almost third order accuracy and is well suited for implementation on unstructured meshes due to its local reconstruction. Attention has been also paid to formulate the source term of the bottom topography in a way exactly balancing the numerical flux function to satisfy the C-property in the static case.

Widely used benchmark tests have been computed to verify the proposed numerical model. Compared to other methods reported in the literature, the numerical results of our model look very competitive in accuracy.

The present formulation provides an accurate and robust numerical framework, and more importantly is well suited for unstructured meshes. Thus, it can be a promising base of high accurate models for practical use in river and coastal simulations.

References

[1] R. Akoh, S. Ii, F. Xiao, A CIP/multi-moment finite volume method for shallow water equations with source terms, Int. J. Numer. Method Fluids 56 (2008) 2245.
[2] K. Anastasiou, C.T. Chan, Solution of the 2D shallow water equations using the finite volume method on unstructured triangular meshes, Int. J. Numer. Method Fluids 24 (1997) 1225.
[3] V. Aizinger, C. Dawson, A discontinuous Galerkin method for two-dimensional flow and transport in shallow water, Adv. Water Resour. 25 (2002) 67.
[4] A. Bermudez, M.E. Vazquez-Cendon, Upwind method for hyperbolic conservation laws with source terms, Comput. Fluids 23 (1994) 1049.
[5] J.P. Boyd, Equatorial solitary waves. Part I: Rossby solitons, J. Phys. Oceanography 10 (1980) 1699.
[6] P. Brufau, M.E. Vazquez-Cendon, P. Garca-Navarro, A numerical model for the flooding and drying of irregular domains, Int. J. Numer. Method Fluids 39 (2002) 247.
[7] J. Burguete, P.G. Navarro, Efficient construction of high-resolution TVD conservative schemes for equations with source terms: application to shallow water flows, Int. J. Numer. Method Fluids 37 (2001) 209.
[8] C. Chen, F. Xiao, Shallow water model on cubed-sphere by multi-moment finite volume method, J. Comput. Phys. 227 (2008) 5019.
[9] B.J. Choi, M. Iskandarani, J. Levin, D.B. Haidvogel, A spectral finite-volume method for the shallow water equations, Mon. Weather Rev. 132 (2004) 1777.
[10] P. Colella, P. Woodward, The piecewise parabolic method for gas-dynamical simulations, J. Comput. Phys. 54 (1984) 174.
[11] K.S. Erduran, V. Kutija, C.J.M. Hewett, Performance of finite volume solutions to the shallow water equations with shock-capturing schemes, Int. J. Numer. Method Fluids 40 (2002) 1237.
[12] C. Eskilsson, S.J. Sherwin, A triangular spectral/hp discontinuous Galerkin method for modeling 2D shallow water equations, Int. J. Numer. Method Fluids 45 (2004) 605.
[13] J.M. Gallardo, C. Pares, M. Castro, On a well-balanced high-order finite volume scheme for shallow water equations with topography and dry areas, J. Comput. Phys. 227 (2007) 574.
[14] T. Gallouet, J.M. Herard, N. Seguin, Some approximate Godunov schemes to compute shallow-water equations with topography, Comput. Fluids 32 (2003) 479.
[15] F.X. Giraldo, T. Warburton, A high-order triangular discontinuous Galerkin oceanic shallow water model, Int. J. Numer. Method Fluids 56 (2008) 899.
[16] <http://marine.rutgers.edu/po/index.php?model=test-problems&title=soliton&page=param_conds>.
[17] E. Hanert, D.Y. Le Roux, V. Legat, E. Deleersnijder, An efficient Eulerian finite element method for the shallow water equations, Ocean Model. 10 (2005) 115.
[18] S. Ii, M. Shimuta, F. Xiao, A 4th-order and single-cell-based advection scheme on unstructured grids using multi-moments, Comput. Phys. Commun. 173 (2005) 17.
[19] S. Ii, F. Xiao, CIP/multi-moment finite volume method for Euler equations: a semi-Lagrangian characteristic formulation, J. Comput. Phys. 222 (2007) 849.
[20] G. Kesserwani, R. Ghostine, J. Vazquez, A. Ghenaim, R. Mose, Application of a second-order Runge-Kutta discontinuous Galerkin scheme for the shallow water equations with source terms, Int. J. Numer. Method Fluids 56 (2008) 805.
[21] G. Kesserwani, R. Mose, J. Vazquez, A. Ghenaim, A practical implementation of high-order RKDG models for the 1D open-channel flow equations, Int. J. Numer. Method Fluids 59 (2009) 1389.
[22] R.J. LeVeque, Balancing source terms and flux gradients in high-resolution Godnov methods: the quasi-steady wave-propagation algorithm, J. Comput. Phys. 146 (1998) 346.
[23] G.F. Lin, J.S. Lai, W.L. Guo, Finite-volume component-wise TVD schemes for 2D shallow water equations, Adv. Water. Resour. 26 (2003) 861.
[24] A. Mohammadian, D.Y. Le Roux, Simulation of shallow flows over variable topographies using unstructured grids, Int. J. Numer. Method Fluids 52 (2006) 473.
[25] S. Noelle, N. Pankratz, G. Puppo, J.R. Natvig, Well-balanced finite volume schemes of arbitrary order of accuracy for shallow water flows, J. Comput. Phys. 213 (2006) 474.
[26] C.W. Shu, Total variation diminishing time discretizations, SIAM J. Sci. Statist. Comput. 9 (1989) 1073.
[27] C.W. Shu, S. Osher, Efficient implementation of essentially non-oscillatory shock-capturing schemes, J. Comput. Phys. 77 (1989) 439.
[28] R. Tanaka, T. Nakamura, T. Yabe, Constructing exactly conservative scheme in a non-conservative form, Comput. Phys. Commun. 126 (2000) 232.
[29] B. van Leer, Towards the ultimate conservative difference scheme 5. 2nd-order sequel to Godunov's method, J. Comput. Phys. 32 (1979) 101.
[30] E.F. Toro, Shock-Capturing Methods for Free-Surface Shallow Flows, John Wiley & Sons Ltd., 2001.
[31] G. Vignoli, V.A. Titarev, E.F. Toro, ADER schemes for the shallow water equations in channel with irregular bottom elevation, J. Comput. Phys. 227 (2008) 2463.
[32] M.E. Vazquez-Cendon, Improved treatment of source terms in upwind schemes for the shallow water equations in channels with irregular geometry, J. Comput. Phys. 148 (1999) 497.
[33] J.W. Wang, R.X. Liu, The composite finite volume method on unstructured meshes for the two-dimensional shallow water equations, Int. J. Numer. Method Fluids 37 (2001) 933.
[34] F. Xiao, Unified formulation for compressible and incompressible flows by using multi integrated moment method: one-dimensional inviscid compressible flow, J. Comput. Phys. 195 (2004) 629.
[35] F. Xiao, R. Akoh, S. Ii, Unified formulation for compressible and incompressible flows by using multi-integrated moments ii: Multi-dimensional version for compressible and incompressible flows, J. Comput. Phys. 213 (2006) 31.
[36] F. Xiao, A. Ikebata, An efficient method for capturing free boundary in multi-fluid simulations, Int. J. Numer. Method Fluid 42 (2003) 187.
[37] F. Xiao, A. Ikebata, T. Hasegawa, Numerical simulations of free-interface fluids by a multi integrated moment method, Comput. Struct. 83 (2005) 409.
[38] F. Xiao, T. Yabe, Completely conservative and oscillation-less semi-Lagrangian schemes for advection transportation, J. Comput. Phys. 170 (2001) 498.
[39] F. Xiao, T. Yabe, X. Peng, H. Kobayashi, Conservative and oscillation-less atmospheric transport schemes based on rational functions, J. Geophys. Res. 107 (2002) 4609.
[40] Y. Xing, C.W. Shu, High order finite difference WENO schemes for a class of hyperbolic systems with source terms, J. Comput. Phys. 208 (2005) 206.
[41] Y. Xing, C.W. Shu, High order well-balanced finite volume WENO schemes and discontinuous Galerkin methods for a class of hyperbolic systems with source terms, J. Comput. Phys. 214 (2006) 567.
[42] T. Yabe, R. Tanaka, T. Nakamura, F. Xiao, Exactly conservative semi-Lagrangian scheme (CIP-CSL) in one dimension, Mon. Weather Rev. 129 (2001) 332.
[43] M.P. Zhang, C.W. Shu, An analysis of and a comparison between the discontinuous Galerkin and the spectral finite volume methods, Comput. Fluids 34 (2005) 581.
[44] D.H. Zhao, H.W. Shen, G.Q. Tabios, J.S. Lai, W.Y. Tan, Finite volume two-dimensional unsteady flow model for river basins, J. Hydrol. Eng. 120 (1994) 863.